Eulerian-Eulerian Simulation of Dense Solid-Gas Cylindrical Fluidized Beds: Impact of Wall Boundary Condition and Drag Model on Fluidization

A. Bakshi*, C. Altantzis, R.B. Bates, A.F. Ghoniem

Massachusetts Institute of Technology, Department of Mechanical Engineering
77 Massachusetts Ave., Cambridge, MA 02139, United States

Abstract

Modeling the hydrodynamics of dense-solid gas flows is strongly affected by the wall boundary condition and in particular, the specularity coefficient ϕ which characterizes the tangential momentum transfer from the particles to the wall. The focus of this study is to investigate the impact of ϕ on the fluidization hydrodynamics using a fully Eulerian description of the solid and gas phases in 3D cylindrical coordinates. In order to quantify this impact, tools for characterizing the bubbling dynamics and solids circulation are developed and applied to both lab-scale (diameters 10 cm and 14.5 cm) and pilot-scale (diameter 30 cm) cylindrical beds. Comparison of simulation predictions with experimental data for different fluidization regimes and particle properties suggests that values of ϕ in the range [0.01,0.3] are suitable for simulating most dense solid-gas flows of practical interest. It is also shown that for this range of ϕ, the fluidization hydrodynamics are not significantly dependent on the choice of ϕ especially as the bed diameter is increased. Additionally, 3D validation of the variable ϕ model by Li and Benyahia [1] shows the bubble diameter predictions to be in excellent agreement with experiment and the average value of ϕ predicted within the range [0.01,0.3]. Quantifying the impact of ϕ and establishing an appropriate range is not only important for accurate simulations at both lab and pilot scales but also validation of models and sub-models for a better understanding of the fluidization phenomenon. Finally, a comparison of the Gidaspow and Syamlal-O'Brien gas-solids drag model shows that the former is more applicable to homogeneous bubbling fluidization ($U/U_{mf} < 4$) while the latter is only suitable for high velocities ($U/U_{mf} > 4$) associated with larger bubbles and slugs.

Keywords: Fluidized bed, two-fluid model, wall boundary condition, bubble dynamics, solids circulation

1. Introduction

Fluidized bed technology is employed in a variety of industrial applications in the chemical and petroleum industries and is especially suitable for large-scale operations since gas-solid mixing provides high heat and mass transfer rates as compared to other means of contacting [2]. The design and performance optimization of fluidized beds continues to be challenging. Obtaining sufficient experimental data is often difficult in the harsh and opaque conditions (high temperature and pressure) most fluidized beds operate at especially the instrumentation. With ever increasing computational power and the development of numerically efficient solvers, the role of Computational Fluid Dynamics (CFD) is, therefore, critical in complementing experimental investigations as a means to understand the flow hydrodynamics and optimize the operation.

Solid-gas flows may be modeled using a combination of Lagrangian and Eulerian models. The most detailed description is the Discrete Particle Model (DPM) or the Lagrangian-Eulerian framework where the solid phase consists of individual particles interacting with each other and the continuous gas phase [3–5]. Current computational resources, however, limit the number of solid particles that can be tracked simultaneously making the approach only feasible for dilute solid-phase flows [6]. The most widely used approach for simulating dense solid-gas flows for industrial-scale applications is the Eulerian-Eulerian framework or the Two Fluid Model (TFM) [7, 8]. By representing both the gas and the solid phases as inter-penetrating continua, the TFM is computationally efficient but requires accurate closure relationships for particle-particle, particle-gas and particle-wall interactions to achieve modeling fidelity [9]. While the particle-particle and particle-gas interactions have been

---

*Corresponding Author
Email address: abakshi@mit.edu, Telephone number: +1 (617) 459-1318

investigated with considerable effort in literature [10–14], the uncertainty regarding the modeling of particle-wall interactions using the Eulerian approach is the central focus of this study, with additional investigation into the suitability of drag models.

It is well documented in literature that particle-wall interactions play a significant role in fluidization predictions [15–17]. This is especially true for small laboratory-scale (cylindrical or thin rectangular) fluidized beds which are commonly used to obtain experimental data for validating numerical models (e.g. [18–20]). On the other hand, implementing the wall boundary condition in numerical simulations based on the Eulerian representation of the solid phase is not trivial and the complexity is compounded by the lack of experimental data. Nevertheless, it has been well accepted that for most applications, a no-slip condition for the gas-phase is appropriate while a partial slip model for the solid phase may be used to capture the particle-wall interactions (collisions and sliding). Several models have been proposed for the solids slip velocity in the TFM (e.g. [21–23]). For the two limiting cases i.e. small friction/all-sliding and large-friction no-sliding, Jenkins [21] derived analytical expressions for the momentum and energy transfer in terms of measurable properties such as the frictional coefficient and the normal and tangential restitution coefficients. In order to make analytical solutions possible though, this theory makes several assumptions for the spatial and velocity distribution of particles close to the walls while neglecting the angular velocity fluctuations [24]. Schneiderbauer et al [22] recently extended this theory for flat, frictional moving walls by including non-steady state effects i.e. the compression and expansion of granular media at the boundaries. While the expressions in [21] are convenient, conditions in bubbling fluidized beds usually operate between these two limits where interpolation is non-trivial and may yield considerable error in the prediction of the slip velocity [1]. The most widely used approach continues to be the Johnson-Jackson model [23] which evaluates the solids slip velocity at the walls based on simple and physically sound arguments.

The Johnson-Jackson boundary condition [23] considers the tangential momentum transferred through particle-wall interactions by (a) Coulomb friction characterized by the frictional coefficient μ and (b) collisions characterized by the normal restitution coefficient e_w and the specularity coefficient ϕ. Several analytical and semi-empirical models have been developed to evaluate μ and e_w in terms of flow parameters such as the impact velocity, impact angle, particle spin and the particle and wall properties [25–29]. While it has been shown that the frictional coefficient significantly affects the collision regime (sliding/non-sliding) [25], fluidization predictions are not sensitive to e_w in the range 0.7-1.0 [1, 30]. On the other hand, direct experimental measurement of ϕ is not possible making it a *tunable* parameter for simulation predictions to fit experimental data. The biggest complexity though is that fluidization metrics such as gas back mixing [15], bubble dynamics [16] and segregation in binary mixtures [17] are particularly sensitive to the choice of ϕ. In fact, Altantzis et al [31] recently showed that for a thin rectangular bed, the choice of ϕ may even alter the fluidization regime; slug formation being characteristic to lower values of ϕ. In general, it has been determined that low values ($\sim 10^{-4} - 10^{-3}$) are suitable for circulating beds [32, 33] while higher values ($\sim$ 0.05-0.5) are appropriate for bubbling beds [15–17, 30]. This suggests that the choice of ϕ is dependent on the flow and particle-wall collision properties and may not be universally applicable [1, 15, 31].

In an attempt to determine ϕ *in situ*, Li and Benyahia [1] used the classic rigid-body theory in conjunction with the semi-analytical model for oblique collisions by Wu et al [29] to obtain ϕ in terms of μ and e_w through numerical integration. The derived polynomial expression was further used in a series of 2D simulations for bubbling and circulating fluidized beds and found to be consistent with trends in literature [34]. While the model itself was derived independent of the choice of coordinate system (2D/3D), it has been shown previously that 2D simulations may yield significantly different predictions as compared to 3D simulations for the same choice of ϕ [16, 31]. In this context, the specularity coefficient *tuned* for 2D simulations may not be applicable to 3D simulations. While there are several studies discussing the impact of the choice of ϕ using 2D simulation predictions (e.g. [17, 30, 34, 35]), there are very few studies which discuss this for the 3D domain (e.g. [15, 16, 31]). The need for the appropriate value of ϕ becomes particularly important for mixing and segregation studies and reactive simulations which are inherently 3D.

Validation of models usually involves comparison of the time averaged bed height and pressure drop at various axial locations between simulations and experiments. These quantities are useful and indicative of the fluidization characteristics but as will be shown in this study, a complete and accurate description of the fluidization may only be possible by quantifying both the solids circulation as well as the bubbling dynamics. Solids circulation may be quantified using the circulation time which is representative of the solids mixing time and inversely related to the solids velocity. Several studies have attempted to measure the solids circulation time and correlate it with the excess gas velocity i.e. U-U$_{\text{mf}}$ (e.g. [36–38]). Measuring the circulation time, however, requires optical access or the use of tracer particles limiting most studies to extremely thin beds. Meanwhile,

2

bubble dynamics may be characterized using bubble statistics describing bubble location (axial/lateral), bubble size and bubble velocity and hence, providing an estimate for the gas motion through bubbles. Bubble statistics are usually computed by a combination of Particle Image Velocimetry (PIA) and Digital Image Analysis (DIA) (e.g. [20, 39]) or more recently, using Electrical Capacitance Tomography (ECT) [19]. Both these metrics are essential for characterizing fluidization in large cylindrical beds for which experimental data is often not available. This becomes especially important in the context of reactive fluidization where an *a priori* estimation of the residence times of gas volatiles and solid fuel is critical for process optimization. While the gas and solids motion in a fluidized bed are inherently coupled, there is no established correlation due to the lack of experimental studies in literature simultaneously measuring the solids velocity and bubble statistics.

In a previous study, Altantzis et al [31] investigated the impact of the wall boundary condition on the fluidization of spherical glass particles in a thin-rectangular bed (50 cm x 0.5 cm), a geometric setup favorable for experimental measurements due to convenient optical accessibility to the fluidized bed material. The authors computed the solids circulation fluxes and times as well as bubbling statistics for a detailed comparison with the digital image analysis measurements reported previously by Sánchez-Delgado et al [36]. They observed significant differences in the fluidization patterns with larger and faster moving bubbles (slugs) and exponentially decreasing circulation time as ϕ was decreased. Interestingly, their comparison of circulation time predictions with experimental measurements revealed that the appropriate ϕ depended on the fluidization regime: ϕ decreased from 0.8 to 0.05 as the inlet gas velocity was increased from 1.5 to 2.5 U_{mf}. However, it has also been shown previously that there are significant differences between dense solid-gas flows through thin rectangular (*pseudo 2D*) beds and cylindrical beds in terms of the bubbling behavior [40] (and hence, the solids circulation) since the flow is confined by the front and back walls in the former. Thus, even though this study elucidates the effect of the wall boundary condition on the hydrodynamics for lab-scale studies on thin-rectangular beds, the high wall surface to bed volume ratio of this setup renders any analysis and consequent inferences unsuitable for application to dense flows in cylindrical beds, especially for studies focused on scaling-up for commercial applications.

The present study is focused on the validation of the boundary condition in cylindrical bubbling fluidized beds and sensitivity of the hydrodynamics to ϕ. After a brief description of the experimental and simulation setups in Sections 2 and 3 respectively, fluidization metrics are developed for cylindrical beds in Section 4. In Section 5, the developed metrics are first used to estimate the suitable range of ϕ by comparing simulation predictions with experimental measurements corresponding to different fluidization regimes and then to quantify the sensitivity of the hydrodynamics in both lab-scale (diameter 14.5 cm) and pilot-scale (diameter 30.0 cm) fluidized beds. Finally, a comparison of the predictions using the variable ϕ model by Li and Benyahia [1] with experimental measurements as well as the suitability of gas-solids drag models are presented. All simulations are performed using *MFiX* (Multiphase Flow with Interface eXchanges), an open-source code developed at the National Energy Technology Laboratory, USA to describe the hydrodynamics in solid-gas systems.

2. Experimental Setup

In order to span a wide range of fluidization regimes (particle properties and inlet gas velocity), simulation predictions are compared with experimental measurements by Rüdisüli et al [20] and Verma et al [19] in Section 5.3 while only the former is considered and scaled-up for the sensitivity study in Section 5.4. In [20], cold fluidization was carried out in a glass column with internal diameter 14.5 cm using alumina particles. The vertical bubble cord length was measured using reflective-type optical probes at a sampling frequency of 400 Hz. Further, bubble velocity was measured using a bubble linking algorithm by measuring the response using two such probes placed 1 cm apart. Meanwhile, Verma et al [19] used a polycarbonate cylindrical tube with internal diameter 0.1 m. The measurements in this setup were done at three cross-sections of the bed using an ultrafast electron beam X-ray scanner acquiring data at 1000 Hz with a high spatial resolution of about 1 mm. The images were then processed using an in-house reconstruction software to reveal time and spatially resolved bubbles. Both setups were operated in the regime of bubbling fluidization using Geldart B particles made of glass, alumina and LLDPE spanning a wide range of particle properties. A summary of all the experimental conditions and particle properties is presented in Tables 1 and 2 respectively.

3. Simulation Setup

3.1. Governing Equations

For the present study, the Two Fluid Model (TFM) is used which describes both the solid and gas phases as inter-penetrating continua. The governing equations, therefore, are similar to those used to describe single-

phase fluid flow. For the case of cold fluidization with no chemical reactions, the continuity equations reduce to

$$\frac{\partial}{\partial t}\left(\varepsilon_k \rho_k\right) + \nabla \cdot \left(\varepsilon_k \rho_k \vec{V}_k\right) = 0 \tag{1}$$

while the momentum equations may be represented as

$$\frac{\partial}{\partial t}\left(\varepsilon_k \rho_k \vec{V}_k\right) + \nabla \cdot \left(\varepsilon_k \rho_k \vec{V}_k \vec{V}_k\right) = \nabla \cdot \bar{\bar{S}}_k - \varepsilon_k \nabla P_g + \varepsilon_k \rho_k \vec{g} + \left(\delta_{km}\vec{I}_{gm} - \delta_{kg}\vec{I}_{gm}\right) \tag{2}$$

$$\delta_{ki} = \begin{cases} 1 & \text{if } k = i \\ 0 & \text{otherwise} \end{cases} \tag{3}$$

where ε, ρ and $\vec{V}$ represent the volume fraction, density and velocity with the subscript k denoting the gas ($k = g$) or solid ($k = m$) phases and $\varepsilon_m = 1 - \varepsilon_g$. The terms $\varepsilon_k \nabla P_g$ and $\varepsilon_k \rho_k \vec{g}$ in Equation 2 represent the buoyancy and gravity forces respectively. The computation of the gas phase stress tensor $\bar{\bar{S}}_g$ is identical as in single-phase fluid flow. Meanwhile, evaluation of the solid phase stress tensor is based on the flow regime, i.e. the local packing fraction of the solid phase in comparison to the critical void fraction ε_g^* typically determined by the maximum packing limit of the solid particles [6]. For particle-dilute pockets of the bed i.e. $\varepsilon_g > \varepsilon_g^*$, inelastic collisions between particles primarily contribute to the stress tensor. This is known as the viscous regime and the stress tensor is evaluated using the Kinetic Theory of Granular Flow (KTGF). In the densely packed regions of the bed i.e. $\varepsilon_g \leq \varepsilon_g^*$, there is enduring contact between the particles (plastic flow regime) and the theory of Schaeffer is employed to account for the frictional effects [41]. Thus, the solids stress tensor may be generally described by

$$\bar{\bar{S}}_m = \begin{cases} -P_m^p \bar{\bar{I}} + \bar{\bar{\tau}}_m^p & \text{if } \varepsilon_g \leq \varepsilon_g^* \\ -P_m^v \bar{\bar{I}} + \bar{\bar{\tau}}_m^v & \text{if } \varepsilon_g > \varepsilon_g^* \end{cases} \tag{4}$$

where P_m is the pressure, $\bar{\bar{\tau}}_m$ is the shear stress with superscripts p and v denoting the plastic and viscous regimes respectively, and the evaluation of the stress tensor $\bar{\bar{S}}_m$ for these two regimes is blended using a hyperbolic tangent function around ε_g^* [6]. The computation of the stress tensor is based on the solid phase pressure and viscosity which are both dependent on the granular temperature Θ [42]. The granular temperature is a measure of the specific kinetic energy of the random fluctuating component of the particle velocity and is computed using the transport equation given by

$$\frac{3}{2}\left(\frac{\partial(\varepsilon_m \rho_m \Theta_m)}{\partial t} + \nabla \cdot \left(\varepsilon_m \rho_m \vec{V}_m \Theta_m\right)\right) = \bar{\bar{S}}_m : \nabla \vec{V}_m + \nabla \cdot \vec{q}_{\Theta_m} - \gamma_{\Theta_m} + \phi_{gm} \tag{5}$$

The transport equation considers the production $\bar{\bar{S}}_m : \nabla \vec{V}_m$, diffusion $\nabla \cdot \vec{q}_{\Theta_m}$, dissipation through inelastic collisions γ_{Θ_m} and to the fluid (viscous) ϕ_{gm} all of which are modeled using the KTGF.

A final closure is required for the fluid-solid drag force $\vec{I}_{gm}$ which plays a significant role in the fluidization phenomenon [6]. For the present study, two drag models have been considered based on the fluidization regime. The Gidaspow drag model combines the Ergun model and the Wen-Yu model for the dense and dilute regimes respectively [14]:

$$\vec{I}_{gm} = \beta \left(\vec{V}_g - \vec{V}_m\right) \tag{6}$$

$$\beta = \begin{cases} 150\frac{\varepsilon_m^2 \mu_g}{\varepsilon_g d_p^2} + 1.75\frac{\varepsilon_m \rho_g |\vec{V}_m - \vec{V}_g|}{d_p} & \text{if } \varepsilon_g \leq 0.8 \\ \frac{3}{4}C_d \varepsilon_g^{-2.65}\frac{\varepsilon_m \varepsilon_g \rho_g |\vec{V}_m - \vec{V}_g|}{d_p} & \text{if } \varepsilon_g > 0.8 \end{cases} \tag{7}$$

$$C_d = \begin{cases} \frac{24}{Re}\left(1 + 0.15Re^{0.687}\right) & \text{if } Re < 1000 \\ 0.44 & \text{if } Re \geq 1000 \end{cases} \tag{8}$$

$$Re = \frac{\rho_g \varepsilon_g d_p |\vec{V}_m - \vec{V}_g|}{\mu_g} \tag{9}$$

On the other hand, the Syamlal-O'Brien drag model evaluates the drag based on the single-sphere drag

function and the terminal velocity correlation for the solid phase [42]:

$$I_{gm} = \frac{3\varepsilon_m \varepsilon_g \rho_g}{4\left(V_{rm}\right)^2 d_p} C_{Ds} \left(\frac{Re}{V_{rm}}\right) |\vec{V}_m - \vec{V}_g| \tag{10}$$

$$Re = \frac{d_p |\vec{V}_m - \vec{V}_g| \rho_g}{\mu_g} \tag{11}$$

where C_{Ds} is the single-sphere drag function while V_{rm} is the ratio of the settling velocity of a multi-particle system to that of a single-particle given by

$$V_{rm} = 0.5A - 0.03Re + \sqrt{\left(0.03Re\right)^2 + 0.03Re\left(2B - A\right) + 0.25A^2} \tag{12}$$

where parameters A and B are dependent on the local void fraction and empirical coefficients c_1 and d_1 tuned to recover the experimentally observed minimum fluidization velocity U_{mf} [42].

Although both the models are eventually fitted using experimental data, the Gidaspow model is based on pressure drop correlations in a homogeneously fluidized or packed bed while the Syamlal-O'Brien model is derived using the terminal velocity correlations, suggesting selective suitability of these models. Although differences in the predictions have been noted previously (e.g. [43–46]), there has been no study extensively investigating the suitability of these models with varying bed geometries, particle properties and fluidization regimes. Through simulations conducted as part of this study, it is suggested that the Gidaspow model is more applicable to homogeneous bubbling fluidization (U/U$_{mf}$ <4) while the Syamlal-O'Brien model is more suited to faster fluidization and slugging (U/U$_{mf}$ >4). While choosing an inappropriate gas-solids drag model is likely to weaken the validation study, the mechanism and dependency of fluidization metrics on ϕ and any qualitative discussion presented in Section 5 remain unaltered with the choice of the drag model. A more elaborate justification is presented in Section 5.6 while more details regarding the governing equations and the constitutive relations may be found in [42, 47].

3.2. Boundary Conditions

Since the present study focusses on cylindrical fluidized beds, the TFM is solved in the 3D cylindrical coordinates. The advantage with this approach is that the computational grid perfectly aligns with the physical boundaries making simulations accurate while the skewed aspect ratio of the cells makes it computationally more efficient than the Cartesian grid [48].

Using the cylindrical grid, numerical boundary conditions are required both at the walls as well as the grid center, even though there is no physical boundary at the center. While a free-slip condition suffices for the axial velocity and the scalar variables, the radial velocity at the center V_{r0} for both the solid and gas phases at each time step is determined using the surrounding velocity field [48] as

$$\bar{V}_{x,k}(y) = -\frac{2}{N_\theta} \sum_i^{N_\theta} V_{\theta,k} \left(\frac{\Delta r_1}{2}, y, \theta_i\right) \, sin\theta_i \tag{13}$$

$$\bar{V}_z(y) = \frac{2}{N_\theta} \sum_i^{N_\theta} V_{\theta,k} \left(\frac{\Delta r_1}{2}, y, \theta_i\right) \, cos\theta_i \tag{14}$$

$$V_{r=0,k}(y, \theta_i) = \bar{V}_x(y) \, cos\theta_k + \bar{V}_z(y) \, sin\theta_k \tag{15}$$

where V_θ and N_θ are the velocity and number of discretized cells in the azimuthal (θ) direction. More details about the theoretical and implementation aspects of the centerline condition may be found in [48]. Meanwhile, the wall boundary condition, which is the focus of this paper, is specified by a no-slip condition for the gas-phase and the Johnson-Jackson model [23] for the solid phase evaluating the slip velocity ($\vec{V}_{sl}$) and the granular temperature for the solid phase at the walls as

$$\frac{\vec{n} \cdot \left(\vec{S}_c + \vec{S}_f\right) \cdot \vec{V}_{sl}}{|\vec{V}_{sl}|} + \frac{\pi \phi \varepsilon_m \rho_m |\vec{V}_{sl}| g_0 \sqrt{3\Theta}}{6\varepsilon_{m,max}} + N_f tan\delta = 0 \tag{16}$$

$$\frac{\pi \rho_m \varepsilon_m g_0 \phi \sqrt{3\Theta} \vec{V}_{sl}^2}{6\varepsilon_{m,max}} = -\vec{n} \cdot \kappa_m \nabla\Theta - \frac{\pi \varepsilon_m \rho_m g_0 \Theta \sqrt{3\Theta}(1 - e_w^2)}{4\varepsilon_{m,max}} \tag{17}$$

where $\vec{n}$ is the unit vector normal to the wall and $\varepsilon_{m,max}$ is the maximum packing fraction of the solid phase. The radial distribution function g_0 is the average non-dimensional distance between spherical particles and given by

$$g_0 = \left[1 - \left(\frac{\varepsilon_m}{\varepsilon_{m,max}}\right)^{\frac{1}{3}}\right]^{-1} \tag{18}$$

Equation 16 essentially balances forces at the walls by accounting for the stress in the solid phase approaching the walls (first term), the momentum loss through collisions (second term) and the frictional stress characterized by the angle of friction δ. Equation 17 evaluates the solid phase slip velocity u_{sl} using the balance between the fluctuation energy flux characterized by the diffusion coefficient κ_m and dissipation due to inelastic collisions characterized by particle-wall restitution coefficient e_w. Equations 16 and 17 may be solved simultaneously to obtain the $\vec{V}_{sl}$ and Θ at the boundary.

In most numerical simulations, the frictional stress in Equation 16 is combined with the particle-wall collisions term into a single term [1] so that

$$\vec{n} \cdot \mu_m \nabla \vec{V}_{sl} = -\frac{\pi \phi \varepsilon_m \rho_m \vec{V}_{sl} g_0 \sqrt{3\Theta}}{6\varepsilon_{m,max}} \tag{19}$$

which may be solved in conjunction with Equation 17 for the granular temperature at the wall. Thus, the parameters characterizing the particle-wall interactions are e_w and the specularity coefficient ϕ. e_w is a measure of the particle kinetic energy lost during particle-wall collisions but its impact on the fluidization hydrodynamics may be neglected for $e_w \in [0.7, 1]$ [1, 30]. Meanwhile, $\phi \in [0, 1]$ is the fraction of the particle momentum lost in the tangential direction with 0 representing the case for perfectly specular collisions while 1 for perfectly diffuse collisions. By combining the frictional term in Equation 19, ϕ also accounts for the frictional effects when the solid particles are closely packed (typically $\varepsilon_m > 0.5$) at the walls.

3.3. Numerical Approach

The present study is based on the implementation of the TFM using MFiX, an open-source code developed at the National Energy Technology Lab (NETL). The governing equations are first spatially discretized on a staggered grid using the finite-volume technique employing central differencing for the diffusion terms and the superbee flux limiter (TVD scheme) for the convection terms. The discretized equations are then solved using the SIMPLE (Semi-Implicit Method for Pressure Linked Equations) algorithm. In this algorithm, the velocity field is first predicted based on the pressure field from the previous iteration and then iteratively corrected using the continuity (gas phase) and volume fraction correction (solid phase) equations to maintain incompressibility of both phases. The granular temperature equation is solved once the conservative velocity field at each time step is established. The forward Euler approach is used for time marching with a variable time step to balance the stability and the total computational time; typical values range from 10^{-6}s to 10^{-4}s. More details regarding the numerical algorithm can be found in [49].

4. Fluidization Metrics

While time average predictions such as the gas pressure and the void fraction in the fluidized bed are useful for describing the fluidization, these parameters undermine the instantaneous motion of the solid and gas phases and hence, do not provide the complete description of the hydrodynamics. In this context, bubble statistics and solid phase circulation become essential metrics for accurately characterizing the fluidization especially for mixing and reactive studies. As will also be shown later, some of these metrics may be significantly sensitive to the choice of specularity coefficient even when some of the time mean predictions may reveal little differences.

4.1. Bubble dynamics

Bubble statistics are obtained by a two-step process. Digital Image Analysis (DIA) is first applied by converting a series of 2D images (vertical or cross sectional slices) to grey-scale using ImageJ (http://rsbweb.nih.gov/ij/) with the bubble void threshold set at 0.7 [19]. While using cross-sectional slices for bubble analysis, $d_b = \sqrt{4A_b/\pi}$ is used as the equivalent bubble diameter. For the case of vertical slices, bubbles in contact with the free surface and the boundaries are excluded from the analysis to avoid any ambiguity and the vertical chord length is used as the bubble diameter [20]. Next, Lagrangian Velocimetry Technique (LVT) is applied to obtain

bubble velocities. This algorithm numbers the bubbles in every frame based on their lateral and axial locations and then computes the bubble velocities using the displacement of corresponding bubbles in consecutive frames. To prevent erroneous linking of bubbles, a successfully linked bubble p between two frames i and $i+1$ must satisfy the conditions:

$$y_{p,i+1} - y_{p,i} > 0 \qquad |x_{p,i+1} - x_{p,i}| < c \qquad (20)$$

i.e. only bubbles *moving* upwards and within a lateral distance c are linked. The constant c is hard-coded into the algorithm through trial-error and in general, depends on the frequency of data sampling. For such applications, the accuracy of the bubble statistics is likely to increase with higher data sampling frequency since erroneous bubble linking due to excess bubble activity (splitting / coalescence) is restricted. Keeping this in mind, images are sampled at 100 Hz over a time span of 27s (2700 frames in total) for all the bubble analysis presented in the subsequent sections.

4.2. Circulation time

The solids circulation flux and circulation time are inversely related and indicative of the solids motion. At any time instant, the solid mass flow upwards (*positive*) is given by

$$\dot{m}_s^+(y,t) = \iint \rho_m \, \varepsilon_m(x,y,z,t) \, v_m^+(x,y,z,t) \, dA^+ \qquad (21)$$

$$v_m^+(x,y,z,t) = \begin{cases} v_m(x,y,z,t) & \text{if } v_m(x,y,z,t) > 0 \\ 0 & \text{otherwise} \end{cases} \qquad (22)$$

$$dA^+ = \begin{cases} dA & \text{if } v_m(x,y,z,t) > 0 \\ 0 & \text{otherwise} \end{cases} \qquad (23)$$

where v_m is the axial velocity component of $\vec{V}_m$, dA is the discretized area and the superscript '+' denotes that only cells with upwards (positive) flow have been considered. It follows that the time and cross-section averaged positive circulation (mass) flux and velocity may be computed using

$$J_c^+(y) = \left\langle \frac{1}{A^+(y)} \iint \rho_m \, \varepsilon_m(x,y,z,t) \, v_m^+(x,y,z,t) \, dA^+ \right\rangle \qquad (24)$$

$$\bar{v}_s^{\,+}(y) = \left\langle \frac{\iint \varepsilon_m(x,y,z,t) \, v_m^+(x,y,z,t) \, dA^+}{\iint \varepsilon_m(x,y,z,t) \, dA^+} \right\rangle \qquad (25)$$

where $A^+(y) = \iint dA^+$. Note that while using the cylindrical grid, dA^+ must account for the non-uniformity of the cells in the domain. Using the average solids velocity, the positive circulation time between two axial locations y_1 and y_2 obtained using

$$t_c^+(y_1,y_2) = \int_{y_1}^{y_2} \frac{dy}{\bar{v}_s^{\,+}(y)} \qquad (26)$$

represents the average time taken by solid particles to reach y_2 from y_1. The analysis can be repeated for negative circulation and the total circulation time t_c then given by

$$t_c(y_1,y_2) = t_c^+(y_1,y_2) + t_c^-(y_1,y_2) \qquad (27)$$

represents the mixing time scale. More details regarding the formulation and implementation of the DIA and LVT algorithms for the bubble motion and circulation metrics for the solids motion can be found in [31].

5. Results and Discussion

In Section 5.1, a grid refinement study is presented based on the comparison of various fluidization metrics using different grid resolutions. Using the optimum grid resolution obtained for the lab-scale setup [20], a comparison of bubble statistics using axial and cross-sectional slices is presented in Section 5.2. By comparing bubble diameters predicted using simulations with experimental measurements [19, 20], the suitable range of ϕ is first obtained in Section 5.3 followed by a sensitivity study in Section 5.4. The validation study is then extended to the variable ϕ model by Li and Benyahia [1] in Section 5.5 and finally, the suitability of the two drag models is discussed in Section 5.6.

5.1. Resolution Study

Choosing the optimum grid resolution for small-scale fluidized beds is a non-trivial task. While coarse grids may not capture the hydrodynamics accurately, extremely fine grids may violate the continuum assumption of the TFM resulting in slow convergence and questionable predictions. Keeping the continuum assumption [48] in mind, the grid resolution study presented in Figure 1 considers 16-24 radial cells ($\sim$ 10-15 d_p), 12-16 azimuthal cells and 200-300 axial cells ($\sim$ 11-17 d_p). For each case, a non-uniform grid is employed to prevent excessively small cells at the center while maintaining a high resolution at the walls [48]. In general, all grids show similar predictions with a maximum deviation of about 10%. Evidently, the differences in the predictions using different grid resolutions are more distinct while investigating the solids and gas motion and indistinguishable in the time-average void fraction and pressure profiles. As a compromise between modeling fidelity and computational cost, the resolution $20 \times 200 \times 12$ is chosen to simulate the setup [20]. Time instant snapshots using this resolution are visualized in Figure 2, which shows that smaller bubbles are formed near the distributor which coalesce and form bigger bubbles eventually erupting into the splash zone. Although not shown for the sake of brevity, a similar analysis is used to choose the grid resolution for simulations presented in Sections 5.3.2 and 5.4.2. A summary of the optimal grid resolutions for all studies is presented in Table 3.

5.2. Bubble Statistics Using 2D Slices

Bubble statistics for the present study are obtained using 2D slices in the cylindrical column: vertical slices along the axis or cross-sectional slices. Figure 3 shows that the increase in the vertical chord length of bubbles positively correlates with the increase in the bubble diameter obtained using cross-sectional slices between y=0.23m and y=0.55m for all values of ϕ. While smaller bubbles tend to be more spherical in shape, larger bubbles or slugs are typically elongated, especially for lab-scale setups. This is evident between y=0.4m and y=0.5m where a significant difference in the two diameters is observed. On the other hand, the bubble count from a vertical slice is significantly less than the bubble count from cross-sectional slices since the vertical slice does not capture the bubbles ahead of / behind the particular frame. Nevertheless, this comparison shows that the trends captured by both approaches are qualitatively similar and the final choice depends on the experimental setup used for measurement (e.g. optical probes measure vertical chord length [20] and X-ray imaging measures cross-sectional diameter [19]). Note that all results are derived from 3D simulations and '2D Slices' only refer to the dimensionality of data post-processing.

5.3. Validation

As detailed in Section 3.2, the boundary condition for the TFM is specified using the Johnson-Jackson model where the tangential momentum loss of the particles to the walls is characterized through the specularity coefficient ϕ. Estimating the appropriate ϕ is not only critical for predicting the hydrodynamics accurately but also for validating fluidization models and sub-models. For the present study, five different values of ϕ in the range [0.0005-0.3] are used and simulation results using these values are compared with experimental data from different studies [19, 20]. These studies are chosen not only to cover a wide range of particle properties and fluidization regimes but also because of the different techniques employed for bubble diameter measurement.

5.3.1. Validation study based on Rüdisüli et al [20]

A comparison of the bubble diameters predicted using simulations with experimental measurements is shown in Figure 4 for U/U_{mf}= 2.3, 3.5, 4.6 and 6.8. As mentioned in Section 3.1, the Gidaspow gas-solids drag model (Equation 6-9) is used for U/U_{mf}= 2.3 and 3.5, while the higher velocities are simulated using the Syamlal-O'Brien model (Equations 10-12). Bubble diameter is measured in terms of the vertical chord length with the constraint that only bubbles longer than 1 cm and radially located 5 cm from the walls are considered to replicate the experimental setup. In general, there is better agreement between the predictions using higher values of $\phi = 0.01$-0.3 for all the inlet velocities while bubble velocities for all ϕ, presented in Figure 5, are in good agreement with experimental findings considering the 20% error margin reported in [20]. The standard deviation in the bubble diameters predicted by simulations is between 40-60% (depending on the superficial gas velocity and axial location) which is in qualitative agreement with the large scatter of bubble diameters reported in [20].

5.3.2. Validation study based on Verma et al [19]

For this study, the bubble diameter at any axial location is obtained as $\sqrt{4A_b/\pi}$ where A_b is the cross-sectional bubble area. For the range of particles detailed in Table 2, a comparison of the bubble diameters predicted using simulations with experimental measurements [19] is shown in Figure 6. In this case, predictions using higher values of $\phi = 0.01\text{-}0.3$ show significantly better agreement with experimental measurements. Predictions are also visibly more sensitive to the choice of ϕ because the column used in this study is smaller (diameter 10 cm) and hence, wall effects are expected to play a stronger role in the fluidization process. Note that the Gidaspow drag model (Equations 6-9) is used for all the cases in this study since $U/U_{\mathrm{mf}} \in [1.25,3.0]$.

Overall, based on the comparison between simulations and both experimental studies encapsulating a wide range of particle properties and fluidization regimes (1.25-6.80 U_{mf}), it is evident that higher values of ϕ in the range [0.01-0.3] are appropriate for modeling dense solid-gas flows. A more accurate estimate may only be possible if sufficient and more reliable experimental data is available for different particle properties and fluidization regimes, especially circulation measurements (flux or time) in addition to bubble statistics.

5.4. Impact of Specularity Coefficient

While in the previous section it is shown that $\phi \in [0.01,0.3]$ is the appropriate range for most cases of bubbling fluidization, it is also essential to quantify the sensitivity of different fluidization metrics to the choice of ϕ, especially within this range. In this section, simulation predictions using two beds are presented: lab-scale fluidized bed of diameter 14.5 cm based on the experimental setup [20] in Section 5.4.1 and a pilot-scale fluidized bed of diameter 30 cm in Section 5.4.2. The latter is simply an extension of the lab-scale study with identical particles and inlet gas velocities and is presented as an illustration of the wall effects in pilot-scale beds. Bubble statistics for both these cases are derived based on images obtained from vertical slices along the axis, as discussed in Section 5.2. While simulations for both the columns were run for four superficial velocities (9.43, 14.35, 18.86, 27.88 cm/s), only results using U=18.86 cm/s ($U/U_{\mathrm{mf}} = 4.6$) are presented for brevity, after it was verified that the trends are similar in all cases.

5.4.1. Lab-Scale Fluidized Bed

Five specularity coefficients are selected to study the impact of the boundary condition on the fluidization of alumina particles (Table 2) in a column of diameter 14.5 cm [20]. In Figure 7, it is shown that while global parameters like the time average void fraction and gas pressure predictions are similar (within 6%), the average bubble diameter and bubble count profiles show significant differences (average ranges 13% and 31% respectively). For ϕ=0.3, higher frequency of bubbles is observed close to the distributor forming bigger bubbles near the eruption surface suggesting higher gas up-flow through bubbles as compared to the case of ϕ=0.0005.

Figure 8 shows the positive and negative circulation fluxes and times as defined in Equations 24-27. Both J_c^+ and J_c^- increase as ϕ is decreased and an interesting segregation of profiles is observable with similar predictions using ϕ=0.0005,0.001 while those using ϕ =0.01-0.3 almost collapse suggesting that ϕ may be classified as being *low* valued (0.0005,0.001) or *high* valued (0.01-0.3). These trends may be further explained using Figure 9 which shows the time and azimuthally averaged near-wall local positive velocity v_s^+ and negative velocity v_s^- i.e. at the axial velocity cell center $r_{i+1/2}$

$$v_s^+ \left(r_{i+1/2}, y\right) = \left\langle \frac{\iint\limits_{[r_i, r_{i+1}]} \varepsilon_m \, v_m^+ \, dA^+}{\iint\limits_{[r_i, r_{i+1}]} \varepsilon_m \, dA^+} \right\rangle \tag{28}$$

and likewise for the negative velocity. Both v_s^+ and v_s^- profiles at different axial positions in the bed show that as ϕ is decreased, the particle wall-slip velocity (magnitude) increases due to lower tangential momentum losses on particle-wall collisions. The trend is similar in the near-wall region explaining the increase in $J_c^{+/-}$ as ϕ is decreased. Further, the disparity between $v_s^{+/-}$ profiles predicted using different values of ϕ is likely to depend on the near-wall solids concentration: the higher the solids concentration, the more the momentum dissipation due to friction between the particles resulting in lower disparity in the velocities predicted. Higher up in the bed, formation of large bubbles/slugs, and consequently the increased bubble velocities, results in a more rapid flow close to the walls (as compared to the flow close to the distributor) amplifying the effect of the particle-wall interactions (and the seemingly separation of near-wall velocity profiles). Overall, the segregation in the $J_c^{+/-}$ profiles based on ϕ (low / high value) may be directly attributed to the segregation in the particle wall-slip and near-wall velocity predictions especially at the axial locations y=0.4 m and y=0.5 m.

Figure 8 also shows that the positive solids circulation time t_c^+ is significantly less sensitive to the choice of ϕ as compared to the negative solids circulation time t_c^-. For instance, at y=0.6 m, t_c^+ decreases from 1.84 s to 1.56 s (15%) as ϕ is decreased from 0.3 to 0.0005, while t_c^- decreases from 2.90 s to 2.09 s (28%), although the change within the suitable range $\phi \in [0.01,0.3]$ is significantly less (about 8%). Choosing lower values of ϕ (0.0005,0.001) for such simulations could thus, lead to 50-80% error in the circulation flux or 15-30 % error in the circulation time predictions. Overall, based on Figures 7 and 8, it is also evident that the bubble dynamics and solids circulation are inherently related: higher gas flow through bubbles (ϕ=0.01-0.3) leaves lower gas momentum available for exchange in the emulsion, and hence, lower circulation flux. However, a more quantitative correlation linking the two metrics may only be established on validation with experimental data simultaneously measuring both these metrics. Note that this correlation of increased gas flow through bubbles with decreased solids circulation is in contradiction to the bubbling fluidization simulations in thin rectangular beds, presented by Altantzis et al [31], where the increase in gas bypass (bubble diameter) also corresponds to an increase in the circulation flux: due to the presence of the front and back walls, bubble growth forces the solid particles laterally instigating higher circulation. They also reported significant differences in circulation flux for low superficial gas velocities (U/U$_{\text{mf}}$) with varying ϕ, while in cylindrical bed simulations presented here, the differences at low velocities (2.3 U$_{\text{mf}}$ in this section and 1.25 U$_{\text{mf}}$ in Section 5.3.2) are less prominent.

Meanwhile, time and azimuthally averaged void fraction contour plots for the case of U/U$_{\text{mf}}$=4.6 ($\phi = 0.0005$, 0.01 and 0.3) are shown in Figure 10. While the solid-phase distribution isn't significantly affected when ϕ is decreased from 0.3 to 0.1 suggesting that fluidization hydrodynamics aren't sensitive to the choice of ϕ in the range [0.01,0.3], it is interesting to see a distinct change when ϕ is further decreased to 0.0005. For ϕ=0.0005, faster solids down-flow due to lower wall resistance, as also indicated in Figure 9, results in a more uniform distribution of solid particles in the bed which consequently tends to decrease the bubble frequency. The overall distribution of the solid phase may be critical to fluidized bed applications and such insights are lost on cross-sectional averaging (e.g. Figure 7 which reveals similar void fraction profiles for all ϕ).

Based on the results presented in this section, it is straightforward to see that the choice of ϕ affects the down-flow of particles along the walls and the distribution of solid particles in the bed consequently altering the bubble dynamics. Bubble statistics and solids circulation metrics are useful metrics for quantifying the fluidization and in particular, circulation time measurements (or predictions) may be of particular interest to both experimental as well as computational studies since these represent the mixing time-scales in the bed. The sensitivity of the fluidization metrics to the choice of ϕ in the range 0.01-0.3 (suitable) is not significant, suggesting that any $\phi \in [0.01,0.3]$ is workable for practical applications of bubbling fluidization.

5.4.2. Pilot-Scale Fluidized Bed

In this section, the analysis presented in Section 5.4.1 is extended to fluidization of alumina particles in a pilot-scale fluidized bed of diameter 30 cm. The void fraction distribution along an axial slice in the bed center at different time instants is shown in Figure 11. On visual inspection, it is evident that unlike the case of a lab-scale fluidized bed, bubbles are less constrained to form and move upwards along the bed center. This is also reflected in the time and azimuthally averaged void fraction profiles for the specific case of ϕ=0.1 and U=18.86 cm/s shown in Figure 12. The solid phase is more uniformly distributed in the pilot-scale fluidized bed as compared to the lab-scale fluidized bed where bubbles predominantly move through the center restricting the bulk of the solid particles closer to the walls. Further comparison with Figure 2 also reveals that the bubble through-time is significantly shorter suggesting faster fluidization in the pilot-scale bed, consistent with findings in literature [50]. All these observations may be attributed to the increase in bed diameter and the corresponding reduction in the wall effects on the hydrodynamics (lower surface area-volume ratio).

Impact of the choice of ϕ on the gas-phase and solid-phase metrics are presented in Figures 13 and 14 respectively. As in the lab-scale fluidized bed, the bubble count from simulations using values of $\phi \in [0.01,0.3]$ is significantly higher than from simulations using values 0.0005 and 0.001. Both J_c^- and J_c^+ increase with decreasing ϕ, similar to the smaller bed. Meanwhile, the bubble diameter predictions seem to be less sensitive to the choice of ϕ. While a decrease in the bubble diameter must be expected with increasing bed diameter [50], the bubble diameter predictions could also be limited by the 2D bubble detection algorithm which cannot map the azimuthal movement of bubbles in large beds. For an accurate analysis in this case, 3D bubble detection and tracking techniques must be employed (e.g. [51]).

The dependency of the circulation times between the distributor (y=0 m) and y=0.6 m on ϕ for different U/U$_{\text{mf}}$ is shown in Figure 15. As expected, for the lab-scale fluidized bed, the total circulation time t_c decreases with increasing inlet gas velocity due to faster fluidization and mixing. The sensitivity of the metric to the

choice of ϕ is representative of the wall-effects and is reflected by the slope of the line. It is interesting to note that while t_c^+ remains largely unaffected by the choice of ϕ, t_c^- increases significantly as ϕ in increased. This is not surprising since the down-flow of the solid phase is primarily along the walls and hence, is strongly influenced by the choice of ϕ. Comparison between simulation prediction from the lab-scale and pilot-scale beds reveals that for the latter, the circulation times are significantly shorter and less sensitive to the choice of ϕ since the wall surface area-volume ratio is reduced. Interestingly for U/U$_{mf}$=4.6, t_c^+ and t_c^- for the pilot-scale fluidized bed are of similar magnitude ($t_c^+ \in$[1.42s,1.66s] and $t_c^- \in$[1.73s,1.96s]) unlike the lab-scale bed where t_c^- is about 50% higher than t_c^+ on average. This observation may be a consequence of decreasing wall effects with increasing bed diameter but can only be verified with more simulations using larger bed diameters.

While simulation predictions in the pilot-scale bed are expectedly less sensitive to the choice of ϕ as compared to the lab-scale bed, wall effects are not insignificant. In fact, previous studies indicate that free bubbling may only be possible if the maximum bubble diameter-bed diameter ratio is less than 0.3 [52] (unlike the present study) which may not be possible in beds smaller than 0.5 m [53].

5.5. Variable ϕ model by Li and Benyahia [1]

In their study, Li and Benyahia [1] numerically derived a working expression for ϕ using the normalized solids slip velocity at the wall $r = |\vec{V}_{sl}|/\sqrt{3\Theta}$ and a combination of the friction and particle-wall restitution coefficients $k = \frac{7}{2}\mu(1 + e_w)$ i.e.

$$\phi_{\mathrm{LB}} = \begin{cases} -\frac{7\sqrt{6\pi}(\phi_0)^2}{8k}r + \phi_0 & \text{if } r \leq \frac{4k}{7\sqrt{6\pi}\phi_0} \\ \frac{2}{7}\frac{k}{r\sqrt{6\pi}} & \text{otherwise} \end{cases} \tag{29}$$

where ϕ_0 is the limiting value of ϕ as r→0. In a subsequent study [34], they used this expression in a series of 2D numerical experiments to show the effect of the operating conditions on the particle-wall interactions. While their results are qualitatively consistent with previous findings, the variable ϕ model has not been validated using experimental measurements thus far.

For the present study, Equation 29 is also used to evaluate ϕ *in situ* and simulations are conducted to validate both the model as well as the bubble dynamics. Note that Equation 29 has already been incorporated in the open-source code *MFiX*. A comparison of the average bubble diameters predicted by simulations with experimental measurements by Rüdisüli et al [20] is presented in Figure 16. In general, there is excellent agreement while using the variable ϕ model for all the cases U/U$_{mf}$= 2.3, 3.5, 4.6 and 6.8 and similarly, for simulations modeling the experiments by Verma et al [19] (the latter comparison has not been presented for brevity). $\phi_{\mathrm{LB,avg}}$, which is time and spatially averaged ϕ_{LB}, is presented in Table 4 for all the cases and is in the range [0.01,0.3] consistent with the analysis in Sections 5.3.1 and 5.3.2. Additionally, the axial variation in the time averaged ϕ_{LB} is only about 7% (average standard deviation for all the cases) suggesting an approximately constant value in the bed. Further, $\phi_{\mathrm{LB,avg}}$ decreases with increasing U/U$_{mf}$ for both the beds, which is consistent with previous studies including [31]. To the best of the authors' knowledge, this is the first study validating their model for bubbling fluidized beds using 3D simulations and based on these comparisons, the variable ϕ model may be used for future simulations.

5.6. Comparison of Gas-Solids Drag Models

As noted in Section 3.3, two gas-solid drag models have been used in the present study. The Gidaspow drag model combines the pressure drops from the Ergun equation and the Wen and Yu model [14] to derive the drag coefficient in the dense and dilute pockets of the bed, respectively, while the Syamlal-O'Brien model [42] converts the terminal velocity correlations to drag correlations adjusted to match the experimentally measured minimum fluidization velocity. Thus, the Gidaspow model is more applicable to homogeneous bubbling fluidization [54, 55] while the adjusted Syamlal-O'Brien model is more suited at higher velocities [46]. This is in agreement with the comparison of bubble diameters predicted using the two drag models in Figure 17 for the experimental setup by Rüdisüli et al [20]. Prediction of bubble diameters is accurate using the Gidaspow model for U/U$_{mf}$=2.3 and 3.5, and the Syamlal-O'Brien model for U/U$_{mf}$ >4.

The respective drag forces, based on Equations 6-12 for Alumina particles (d_p=289μm), are computed and shown in Figure 18. Visibly, the Syamlal-O'Brien drag model predicts significantly higher drag force at any given local void fraction and gas-solids slip velocity. Further, Figure 19 indicates that the predicted solids-gas

slip velocity correlates with the bubble distribution i.e. the slip velocity is higher in areas frequented by bubbles and lower close to the walls. Combined with the finding from Figure 18 that the drag force increases with increased slip velocity and decreased void fraction, it is inferred that the drag force (and hence, the momentum exchanged) is significantly high close to the bubble-emulsion interface. Also, since the drag force predicted by the Syamlal-O'Brien model is higher, there is increased momentum exchange which may affect bubble growth adversely and possibly explain the lower overall bubble diameters, as observed earlier in Figure 17. Additionally, the increased drag force for the Syamlal-O'Brien model also explains the increase in the predicted bed height and solids circulation flux increases (not shown for brevity). Interestingly, the Syamlal-O'Brien drag model predicts a finite non-zero drag force in the limiting condition of zero slip velocity (Re→0) which may also suggest its non-suitability to fluidized beds operating near close-packing.

Overall, the Gidaspow model is used for all cases with $U/U_{mf} < 4$ while the Syamlal-O'Brien model is used otherwise. Similar results are observed for the experimental setup by Verma et al [19] and the Gidaspow model is used for the simulations presented in Section 5.3.2 since the operating regime is $U/U_{mf} \in [1.25, 3]$. Figure 17 also distinctly shows that the choice of the drag model has a higher impact on the fluidization hydrodynamics as compared to the choice of ϕ (wall boundary condition). Thus, for accurate simulations, it is imperative that the appropriate gas-solid drag model be used. There is no elaborate study mechanistically linking bubble growth with solids-gas drag and describing the suitability of drag models based on the bed geometry, particle properties and fluidization regimes. While some insights have been presented, the exact mechanism and suitability is outside the domain of the present work but must be addressed in future studies.

6. Conclusion

The boundary condition in the Two-Fluid Model is commonly specified using the Johnson-Jackson model which requires several parameters to characterize the particle-wall collisions and sliding. Since the impact of the frictional and normal restitution coefficients has been reasonably studied in the past, the focus of the present study is two-fold: (a) to establish a suitable range of ϕ for bubbling fluidization in cylindrical beds and (b) to determine the sensitivity of the fluidization process to ϕ within this range. In a previous study by Altantzis et al [31] it was shown that the circulation fluxes and times constitute useful metrics for the description of the solids motion. In addition, the dependence of the fluidization hydrodynamics on the specularity coefficient was investigated and the computational results were validated with previous experimental measurements on a thin rectangular bed. However, as also discussed in Section 5.4.1, analysis and inferences from studies based on thin rectangular beds may not be suitable for cylindrical beds since the flow is confined by the front and back walls in the former resulting in significant differences in the hydrodynamics.

Suitable metrics for fluidization in cylindrical beds are first developed to quantify the bubble motion and the solids circulation since global parameters like the void fraction and gas pressure profiles are shown to not represent the fluidization process completely. Unlike previous studies, validation is then conducted over a wide range of particles (d_p=0.289-1.1 mm, ρ_p=840-2526 kg/m^3) and superficial velocities (U/U_{mf}=1.25-6.80) to indicate that ϕ in the range [0.01,0.3] predicts bubble diameters in good agreement with experimental measurements. Additional simulations using the variable specularity coefficient model by Li and Benyahia [1] also show the bubble diameters to be predicted in excellent agreement not only validating their model but also confirming that the suitable ϕ lies within this range. Next, a comparison of the bubble statistics and solids circulation metrics on a lab-scale bed of diameter 14.5 cm is shown. Although the correlation coupling these two metrics cannot be ascertained due to lack of experimental measurements, it is seen that as ϕ is decreased, the circulation flux (positive and negative) increases due to lower wall resistance, while fewer (and eventually, smaller) bubbles are formed due to increasing presence of solid particles in the bed interiors. The sensitivity of all the metrics to the choice of ϕ within the suitable range [0.01,0.3] is small (much less than the reported experimental error) suggesting that any value in this range may be used in the Johnson-Jackson model to predict most bubbling fluidization cases of practical interest adequately. A more accurate estimate of ϕ may only be possible with a thorough experimental study spanning a wide range of fluidization regimes as well as a more robust computational model incorporating the friction explicitly in the boundary condition.

Simulations for a pilot-scale fluidized bed (diameter of 30 cm) are conducted to investigate the impact of the wall boundary condition and compare the results to those from the lab-scale bed. As the bed diameter is increased, fluidization becomes faster and the tendency of bubbles to grow and move upwards through the

bed center decreases (for the same static bed height). While the exact mechanism of bubble formation and growth in larger beds requires further study, it is evident that the hydrodynamics are affected by the decrease in wall surface area - volume ratio. Similar to the lab-scale bed, the predicted circulation time increases with increasing ϕ, although results are expectedly less sensitive to the choice of ϕ. It is also interesting to note that t_c^+ and t_c^- are of similar magnitude for the pilot-scale bed while the former is significantly shorter for the lab-scale bed. This could be an effect of the increasing bed diameter and change in the bubble flow pattern although more simulations need to be conducted to verify this. Nevertheless, circulation time calculations will help estimate the gas and solid residence times which would be desirable for the design and optimization of pilot-scale / commercial fluidized beds.

Finally, a comparison of the widely used solid-gas drag models suggests that the Gidaspow model is more suitable for lower superficial gas velocities ($U/U_{mf} <4$) while the Syamlal-O'Brien model be preferred for higher velocities. This is because the former is more applicable to homogeneous fluidization, unlike fluidization using higher velocities characterized by slug formation and growth in thin, tall beds (as in the case of most experimental setups). Under these fast bubbling/slugging conditions, the Gidaspow model under-predicts the gas-solids drag force resulting in the over-prediction of bubble diameters. Although some insights into the bubble growth-drag force interaction have been provided, an extensive comparison and suitability of drag models with varying geometrical and operational parameters using 3D simulations is not the focus of the present study but must be addressed in future studies.

7. Acknowledgment

8. References

[1] Tingwen Li and Sofiane Benyahia. Revisiting johnson and jackson boundary conditions for granular flows. *AIChE Journal*, 58(7):2058–2068, 2012.

[2] Daizo Kunii and Octave Levenspiel. *Fluidization Engineering*. 1991.

[3] Y. Tsuji, T. Kawaguchi, and T. Tanaka. Discrete particle simulation of two-dimensional fluidized bed. *Powder Technology*, 77(1):79 – 87, 1993.

[4] B.P.B. Hoomans, J.A.M. Kuipers, W.J. Briels, and W.P.M. van Swaaij. Discrete particle simulation of bubble and slug formation in a two-dimensional gas-fluidised bed: A hard-sphere approach. *Chemical Engineering Science*, 51(1):99 – 118, 1996.

[5] B.H. Xu and A.B. Yu. Numerical simulation of the gas-solid flow in a fluidized bed by combining discrete particle method with computational fluid dynamics. *Chemical Engineering Science*, 52(16):2785 – 2809, 1997.

[6] Nan Xie, Francine Battaglia, and Sreekanth Pannala. Effects of using two- versus three-dimensional computational modeling of fluidized beds: Part i, hydrodynamics. *Powder Technology*, 182(1):1 – 13, 2008.

[7] H Enwald, E Peirano, and A.-E Almstedt. Eulerian two-phase flow theory applied to fluidization. *International Journal of Multiphase Flow*, 22, Supplement:21 – 66, 1996.

[8] Jennifer Sinclair Curtis and Berend van Wachem. Modeling particle-laden flows: A research outlook. *AIChE Journal*, 50(11):2638–2645, 2004.

[9] N.G. Deen M.A. van der Hoef, M. van Sint Annaland and J.A.M. Kuipers. Numerical simulation of dense gas-solid fluidized beds: A multiscale modeling strategy. *Annual Review of Fluid Mechanics*, 40:47–70, 2008.

[10] J.T. Jenkins and S.B. Savage. A theory for the rapid flow of identical, smooth, nearly elastic, spherical particles. *J. Fluid Mech.*, 130:187–202, 1983.

[11] Hayley H. Shen. Stresses in a rapid flow of spherical solid with two sizes. *Particulate Science and Technology*, 2(1):37–56, 1984.

[12] Jianmin Ding and Dimitri Gidaspow. A bubbling fluidization model using kinetic theory of granular flow. *AIChE Journal*, 36(4):523–538, 1990.

[13] M. Syamlal and T.J. O'Brien. Simulation of granular layer inversion in liquid fluidized beds. *International Journal of Multiphase Flow*, 14(4):473 – 481, 1988.

[14] D. Gidaspow. *Multiphase Flow and Fluidization: Continuum and Kinetic Theory Descriptions*. Boston: Academic, 1994.

[15] Tingwen Li, Yongmin Zhang, John R. Grace, and Xiaotao Bi. Numerical investigation of gas mixing in gas-solid fluidized beds. *AIChE Journal*, 56(9):2280–2296, 2010.

[16] Tingwen Li, John Grace, and Xiaotao Bi. Study of wall boundary condition in numerical simulations of bubbling fluidized beds. *Powder Technology*, 203(3):447 – 457, 2010.

[17] Hanbin Zhong, Jinsen Gao, Chunming Xu, and Xingying Lan. {CFD} modeling the hydrodynamics of binary particle mixtures in bubbling fluidized beds: Effect of wall boundary condition. *Powder Technology*, 230(0):232 – 240, 2012.

[18] F. Hernández-Jiménez, J. Sánchez-Prieto, A. Soria-Verdugo, and A. Acosta-Iborra. Experimental quantification of the particlewall frictional forces in pseudo-2d gas fluidised beds. *Chemical Engineering Science*, 102(0):257 – 267, 2013.

[19] Vikrant Verma, Johan T. Padding, Niels G. Deen, J. A. M. (Hans) Kuipers, Frank Barthel, Martina Bieberle, Michael Wagner, and Uwe Hampel. Bubble dynamics in a 3-d gassolid fluidized bed using ultrafast electron beam x-ray tomography and two-fluid model. *AIChE Journal*, 60(5):1632–1644, 2014.

[20] Martin Rüdisüli, Tilman J. Schildhauer, Serge M.A. Biollaz, Alexander Wokaun, and J. Ruud van Ommen. Comparison of bubble growth obtained from pressure fluctuation measurements to optical probing and literature correlations. *Chemical Engineering Science*, 74(0):266 – 275, 2012.

[21] J.T. Jenkins. Boundary conditions for rapid granular flow: Flat, frictional walls. *Journal of Applied Mechanics*, 59:120–127, 1992.

[22] Simon Schneiderbauer, David Schellander, Andreas Lderer, and Stefan Pirker. Non-steady state boundary conditions for collisional granular flows at flat frictional moving walls. *International Journal of Multiphase Flow*, 43(0):149 – 156, 2012.

[23] P.C. Johnson and R. Jackson. Frictional-collisional constitutive relations for granular materials, with application to plane shearing. *J. Fluid Mech.*, 176:67–93, 1987.

[24] Michel Y. Louge. Computer simulations of rapid granular flows of spheres interacting with a flat, frictional boundary. *Physics of Fluids*, 6(7):2253–2269, 1994.

[25] M. Sommerfeld. Modelling of particle-wall collisions in confined gas-particle flows. *International Journal of Multiphase Flow*, 18(6):905 – 926, 1992.

[26] M Sommerfeld and N Huber. Experimental analysis and modelling of particle-wall collisions. *International Journal of Multiphase Flow*, 25(67):1457 – 1489, 1999.

[27] Irma Hussainova, Jakob Kbarsepp, and Igor Shcheglov. Investigation of impact of solid particles against hardmetal and cermet targets. *Tribology International*, 32(6):337 – 344, 1999.

[28] Laurent Labous, Anthony D. Rosato, and Rajesh N. Dave. Measurements of collisional properties of spheres using high-speed video analysis. *Phys. Rev. E*, 56:5717–5725, Nov 1997.

[29] Chuan-Yu Wu, Colin Thornton, and Long-Yuan Li. A semi-analytical model for oblique impacts of elasto-plastic spheres. *Proceedings of the Royal Society A: Mathematical, Physical and Engineering Science*, 465(2103):937–960, 2009.

[30] Xingying Lan, Chunming Xu, Jinsen Gao, and Muthanna Al-Dahhan. Influence of solid-phase wall boundary condition on CFD simulation of spouted beds. *Chemical Engineering Science*, 69(1):419 – 430, 2012.

[31] C. Altantzis, R.B. Bates, and A.F. Ghoniem. 3D Eulerian modeling of thin rectangular gas-solid fluidized beds: Estimation of the specularity coefficient and its effects on bubbling dynamics and circulation times. *Powder Technology*, 270, Part A(0):256 – 270, 2015.

[32] Sofiane Benyahia, Madhava Syamlal, and Thomas J. O'Brien. Evaluation of boundary conditions used to model dilute, turbulent gas/solids flows in a pipe. *Powder Technology*, 156(23):62 – 72, 2005.

[33] Adnan Almuttahar and Fariborz Taghipour. Computational fluid dynamics of high density circulating fluidized bed riser: Study of modeling parameters. *Powder Technology*, 185(1):11 – 23, 2008.

[34] Tingwen Li and Sofiane Benyahia. Evaluation of wall boundary condition parameters for gassolids fluidized bed simulations. *AIChE Journal*, 59(10):3624–3632, 2013.

[35] Chanchal Loha, Himadri Chattopadhyay, and Pradip K. Chatterjee. Euler-euler CFD modeling of fluidized bed: Influence of specularity coefficient on hydrodynamic behavior. *Particuology*, 11(6):673 – 680, 2013.

[36] S. Sánchez-Delgado, C. Marugán-Cruz, A. Soria-Verdugo, and D. Santana. Estimation and experimental validation of the circulation time in a 2d gassolid fluidized beds. *Powder Technology*, 235(0):669 – 676, 2013.

[37] Xianfeng Fan, David J. Parker, Zhufang Yang, Jonathan P.K. Seville, and Jan Baeyens. The effect of bed materials on the solid/bubble motion in a fluidised bed. *Chemical Engineering Science*, 63(4):943 – 950, 2008.

[38] M Stein, Y.L Ding, J.P.K Seville, and D.J Parker. Solids motion in bubbling gas fluidised beds. *Chemical Engineering Science*, 55(22):5291 – 5300, 2000.

[39] S. Sanchez-Delgado U. Ruiz-Rivas A. Soria-Verdugo, L.M. Garcia-Gutierrez. Circulation of an object imersed in a bubbling fluidized bed. *Chemical Engineering Science*, 66(1):78–87, 2011.

[40] D. Geldart. The size and frequency of bubbles in two- and three-dimensional gas-fluidised beds. *Powder Technology*, 4(1):41 – 55, 1970.

[41] D.G. Schaeffer. Instability in the evolution equations describing incompressible granular flow. *Journal of Differential Equations*, 66:19–50, 1987.

[42] Madhava Syamlal, William Rogers, and Thomas J. O'Brien. *MFIX Documentation Theory Guide*, 1993.

[43] Chanchal Loha, Himadri Chattopadhyay, and Pradip K. Chatterjee. Assessment of drag models in simulating bubbling fluidized bed hydrodynamics. *Chemical Engineering Science*, 75(0):400 – 407, 2012.

[44] Pei Pei, Kai Zhang, and Dongsheng Wen. Comparative analysis of CFD models for jetting fluidized beds: The effect of inter-phase drag force. *Powder Technology*, 221(0):114 – 122, 2012.

[45] N. Mahinpey, F. Vejahati, and N. Ellis. CFD simulation of gassolid bubbling fluidized bed: an extensive assessment of drag models. *Computational Methods in Multiphase Flow*, 4:51–60, 2013.

[46] Ehsan Esmaili and Nader Mahinpey. Adjustment of drag coefficient correlations in three dimensional {CFD} simulation of gassolid bubbling fluidized bed. *Advances in Engineering Software*, 42(6):375 – 386, 2011.

[47] S. Benyahia, M. Syamlal, and T.J. OBrien. *Summary of MFIX Equations 2012-1*, January 2012.

[48] A. Bakshi, C. Altantzis, and A.F. Ghoniem. Towards accurate three-dimensional simulation of dense multi-phase flows using cylindrical coordinates. *Powder Technology*, 264(0):242 – 255, 2014.

[49] Madhava Syamlal. *MFIX Documentation Numerical Technique*, January 1998.

[50] Shayan Karimipour and Todd Pugsley. A critical evaluation of literature correlations for predicting bubble size and velocity in gassolid fluidized beds. *Powder Technology*, 205(13):1 – 14, 2011.

[51] C. Sobrino, A. Acosta-Iborra, M.A. Izquierdo-Barrientos, and M. de Vega. Three-dimensional two-fluid modeling of a cylindrical fluidized bed and validation of the maximum entropy method to determine bubble properties. *Chemical Engineering Journal*, (0):–, 2014.

[52] S. Mori and C.Y. Wen. Estimation of the bubble diameter in gaseous fluidized beds. *AIChE Journal*, 21:109–115, 1975.

[53] J. Werther. Influence of the bed diameter on the hydrodynamics of gas fluidized beds. *AIChE Symposium Series*, 70:53–62, 1974.

[54] Dimitri Gidaspow. Hydrodynamics of fluidizatlon and heat transfer: Supercomputer modeling. *Appl. Mech. Rev.*, 39(1):1–23, 1986.

[55] Sreekanth Pannala, Madhava Syamlal, and Thomas J. O'Brien. *Computational Gas-Solids Flows and Reacting Systems - Theory, Methods and Practice*. IGI Global., 2011.

Table 1: Experimental Conditions

Rudisuli et al [20]	
Bed Diameter	0.145 m
Static Bed Height	0.5 m
Measuring Height	0.23 m, 0.45 m
U/U_{mf}	2.3 - 6.8
Verma et al [19]	
Bed Diameter	0.1 m
Static Bed Height	0.2 m
Measuring Height	0.05 m, 0.1 m, 0.2 m
U/U_{mf}	1.25 - 3.0

Table 2: Solid properties: particles used by Rüdisüli et al [20] are used for simulating the 14.5 cm lab-scale and 30 cm pilot-scale beds, while particles used by Verma et al [19] are used in the simulations presented in Section 5.3.2

Type	Density [kg/m^3]	Diameter [mm]	U$_{mf}$ [m/s]
Rüdisüli et al [20]			
Alumina	1350	0.289	0.041
Verma et al [19]			
LLDPE	800	1.1	0.24
Alumina	1040	1.0	0.32
Glass	2526	1.0	0.67

Table 3: Grid resolutions for simulations presented in different sections

Type	Bed ID×Ht	d_P	Grid	Sections
	[mm] x [mm]	[mm]	$[N_r \times N_y \times N_\theta]$	
Lab-Scale [20]	145×1000	0.289	20×200×12	5.3.1, 5.4
				5.5, 5.6
Lab-Scale [19]	100×500	1.0-1.1	12×100×12	5.3.2
Pilot-Scale	300×1000	0.289	40×200×20	5.4

Table 4: Time and bed averaged ϕ predicted using the model by Li and Benyahia (ϕ_{LB}) [1]

Particles	U_{mf} [m/s]	U/U_{mf} [-]	$\phi_{\mathrm{LB,avg}}$ [-]
Rüdisüli et al [20]			
Alumina	0.041	2.3	0.032
		3.5	0.030
		4.6	0.029
		6.8	0.028
Verma et al [19]			
LLDPE	0.24	1.25	0.032
Glass	0.67	2.0	0.027
Alumina	0.32	3.0	0.026
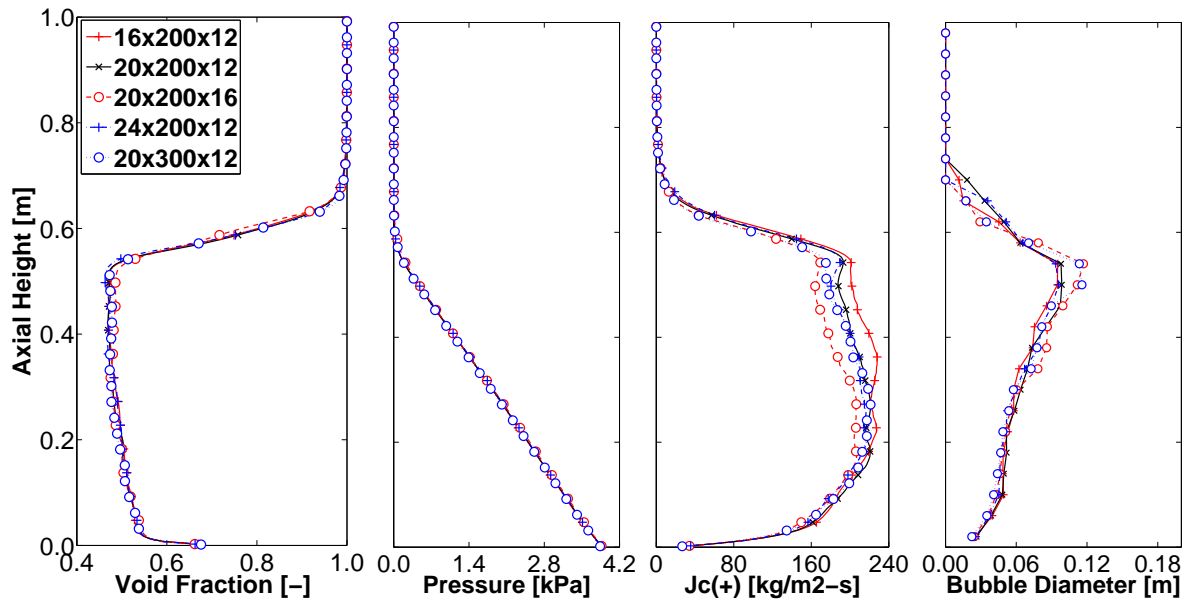
Figure 1: Grid resolution study for the 14.5 cm lab-scale bed based on time average fluidization metrics for U/U$_{\mathrm{mf}}$=4.6 and $\phi = 0.01$ (Cross-sectional resolution $N_r \times N_y \times N_\theta$ represents N_r radial cells, N_y axial cells and N_θ azimuthal cells)
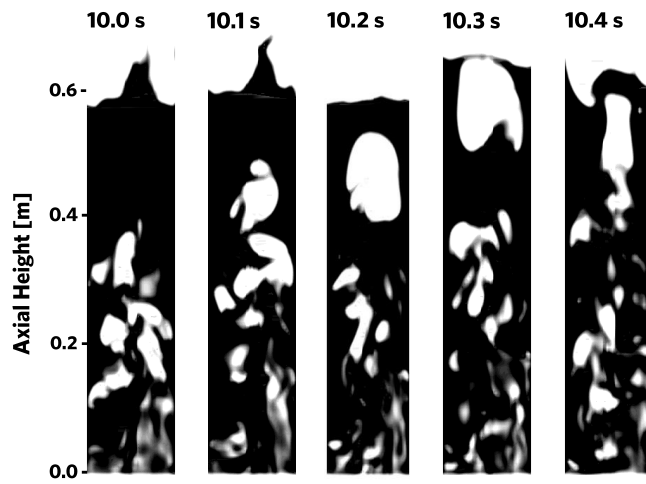
Figure 2: Visualization of bubbles along an axial slice in the bed center for U/U_{mf}=4.6 and $\phi = 0.1$ at different time instants in the 14.5 cm lab-scale bed. Bubble void threshold is set at ε_g=0.7
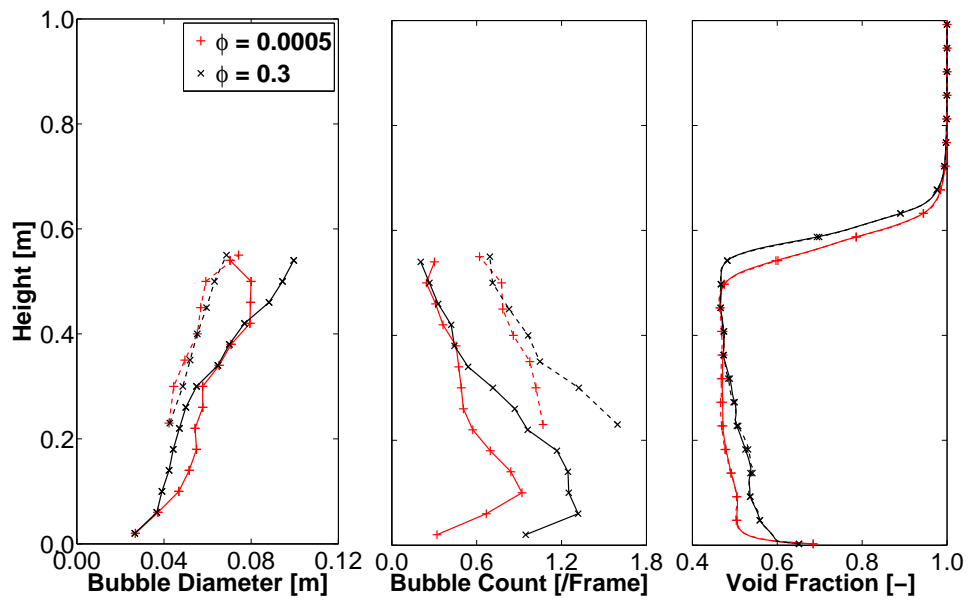
Figure 3: Comparison of bubble statistics and time average void fraction derived from a vertical slice around the axis (—) and cross-sectional slices at different axial locations (- -) for ϕ=0.0005 and 0.3 and U/U$_{\mathrm{mf}}$=4.6 in the 14.5 cm lab-scale bed
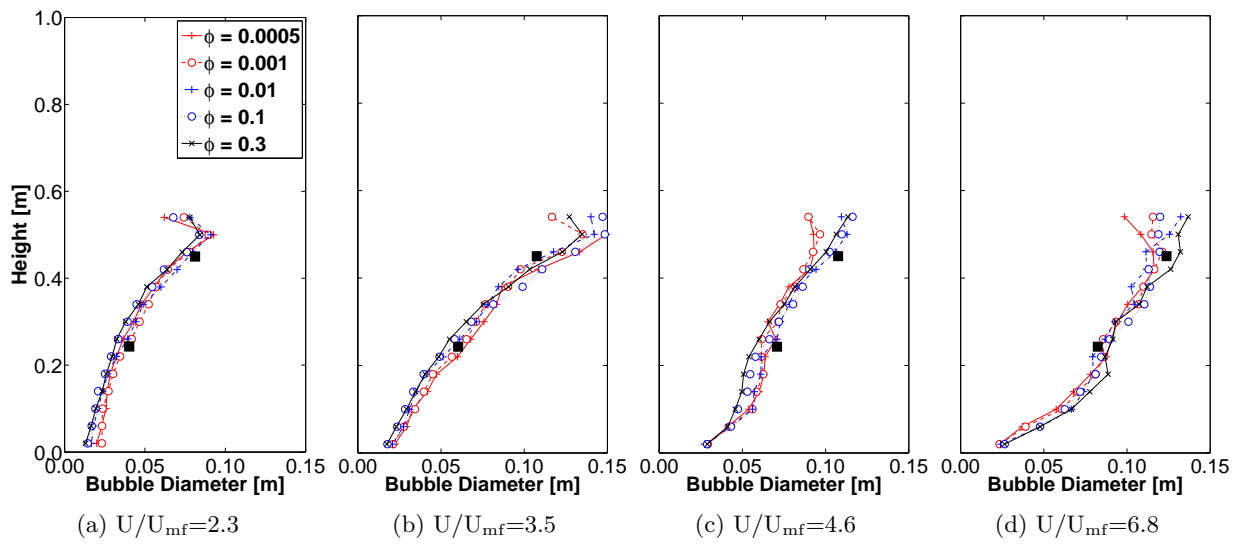
Figure 4: Comparison of average bubble diameter obtained from simulations using different ϕ for U/U_{mf}=2.3, 3.5, 4.6 and 6.8 with experimental measurements (*filled squares*) by Rüdisüli et al [20] at two axial locations y=0.23 m and 0.45 m
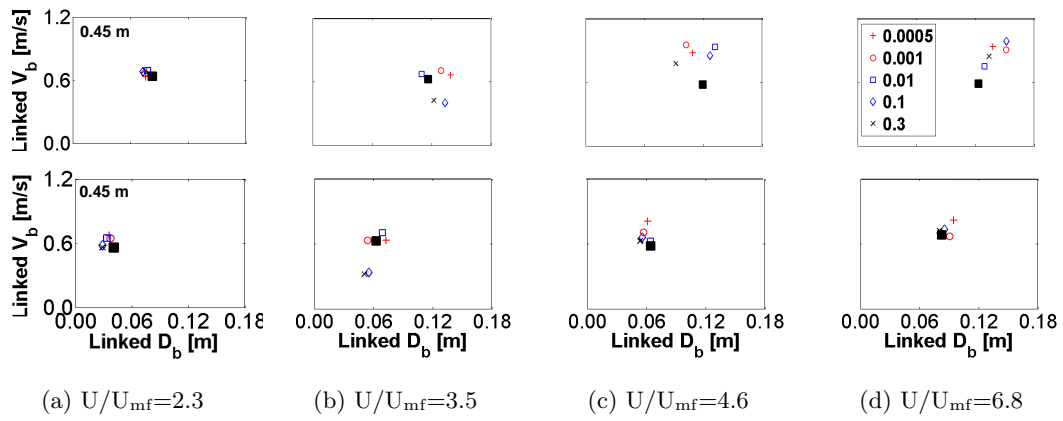
Figure 5: Comparison of linked bubble diameter and velocity obtained from simulations using different ϕ for U/U$_{\mathrm{mf}}$=2.3, 3.5, 4.6 and 6.8 with experimental measurements (*filled squares*) by Rüdisüli et al [20] at two axial locations y=0.23 m and 0.45 m
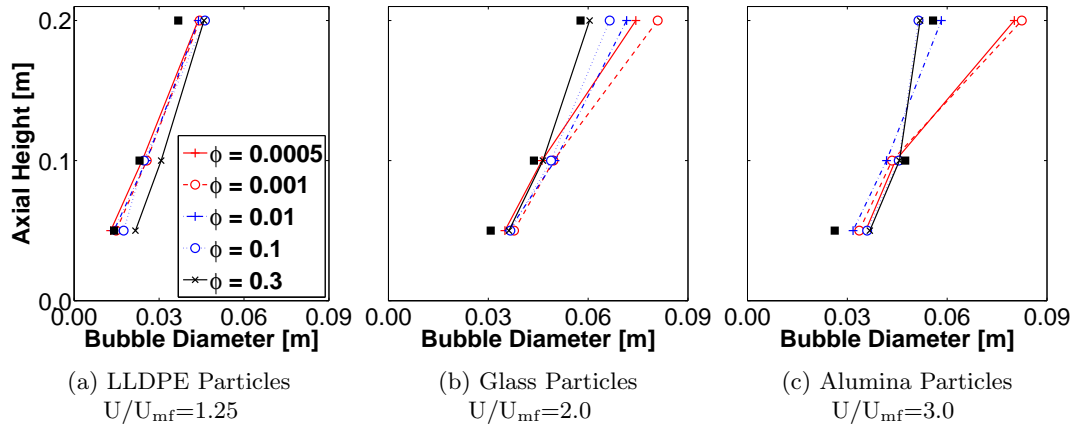
Figure 6: Comparison of average cross-sectional bubble diameter obtained from simulations using different values of ϕ for different particle properties (specified in Table 2) and inlet velocities with experimental measurements (*filled squares*) by Verma et al [19] at three axial locations y = 5 cm, 10 cm and 20 cm
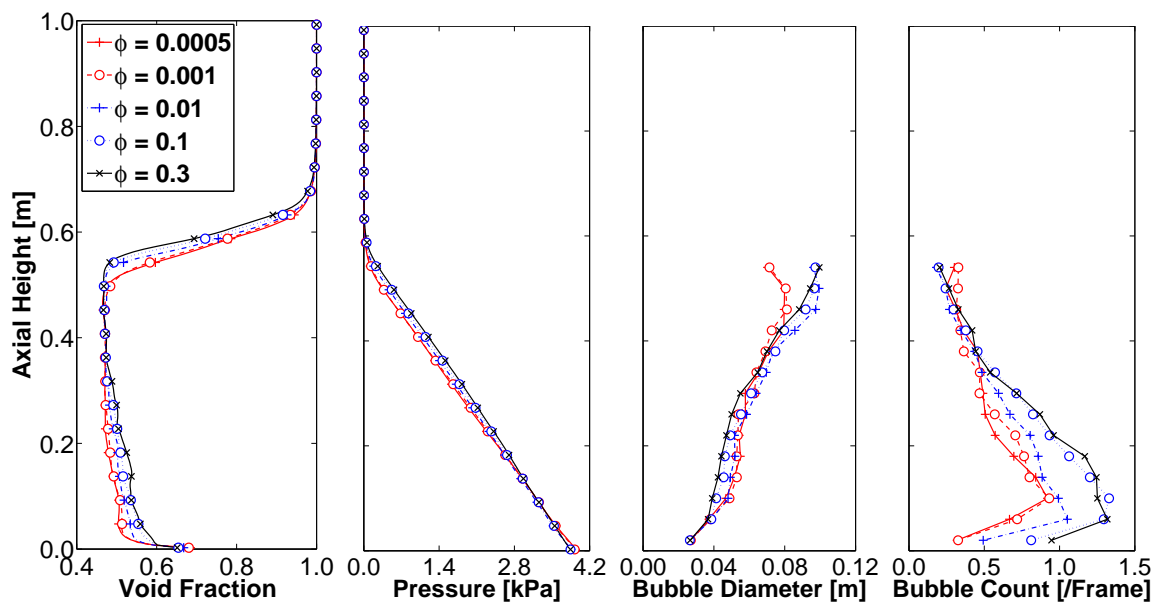
Figure 7: Time average gas-phase metrics using different values of ϕ
for U/U$_{\mathrm{mf}}$=4.6 in the 14.5 cm lab-scale bed

27
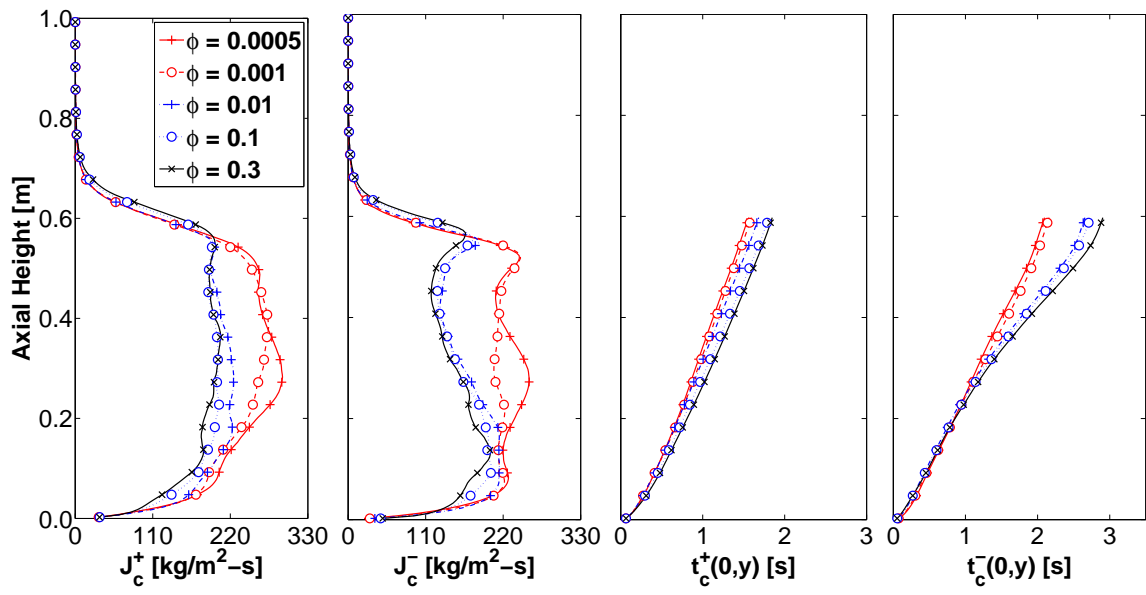
Figure 8: Time average solid-phase metrics using different values of ϕ for U/U$_{\mathrm{mf}}$=4.6 in the 14.5 cm lab-scale bed
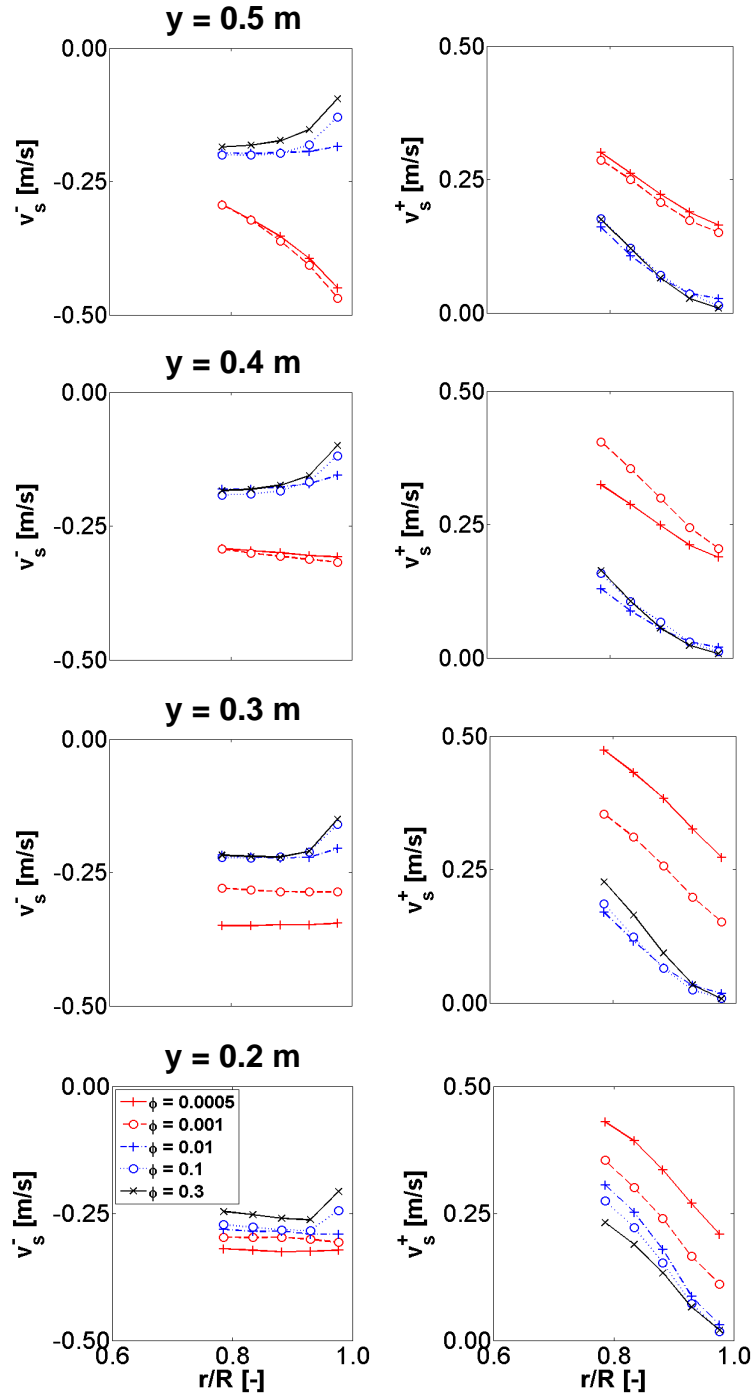
Figure 9: Time and azimuthally averaged near-wall solids negative velocity v_s^- and positive velocity v_s^+ using different values of ϕ for U/U$_{\mathrm{mf}}$=4.6 in the 14.5 cm lab-scale bed. v_s^+ (and similarly v_s^-) has been evaluated using Equation 28
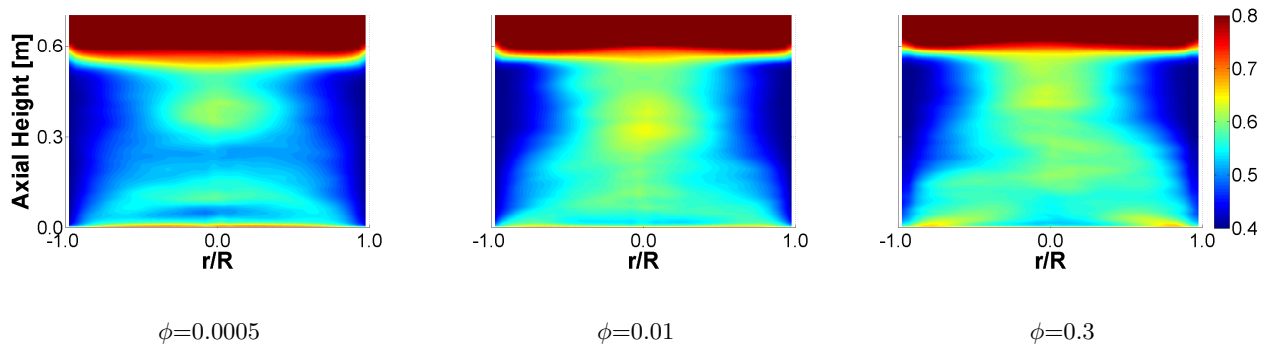
Figure 10: Time and azimuthally averaged void fraction $\varepsilon_g (= 1 - \varepsilon_m)$ for U/U$_{\mathrm{mf}}$=4.6 in the 14.5 cm lab-scale bed for ϕ=0.0005, 0.01 and 0.3
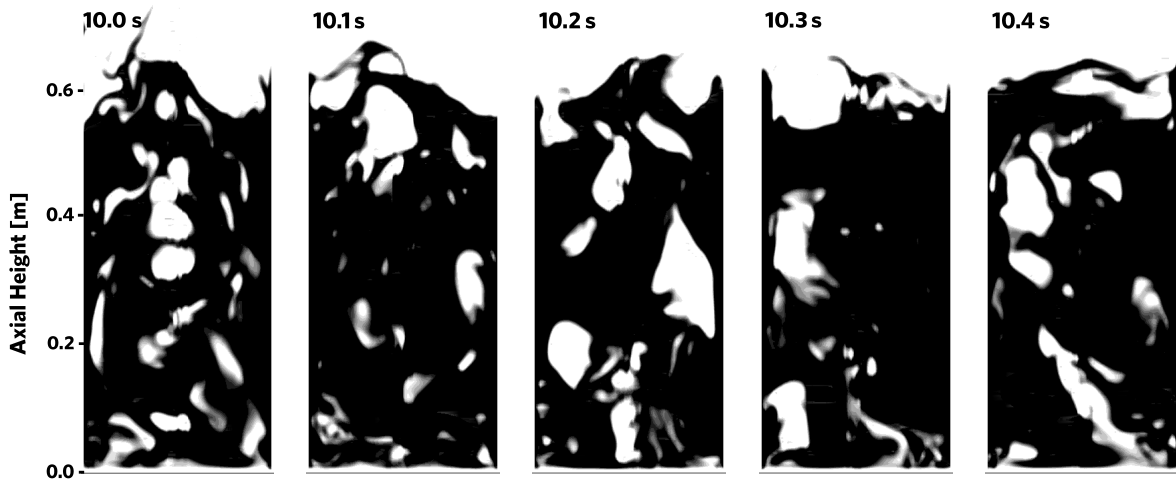
Figure 11: Visualization of bubble dynamics along an axial slice in the bed center for U/U_{mf}=4.6 and $\phi = 0.1$ at different time instants in the 30.0 cm pilot-scale bed. Bubble void threshold is set at ε_g=0.7

Lab-Scale (diameter=14.5 cm)   Pilot-Scale (diameter=30.0 cm)
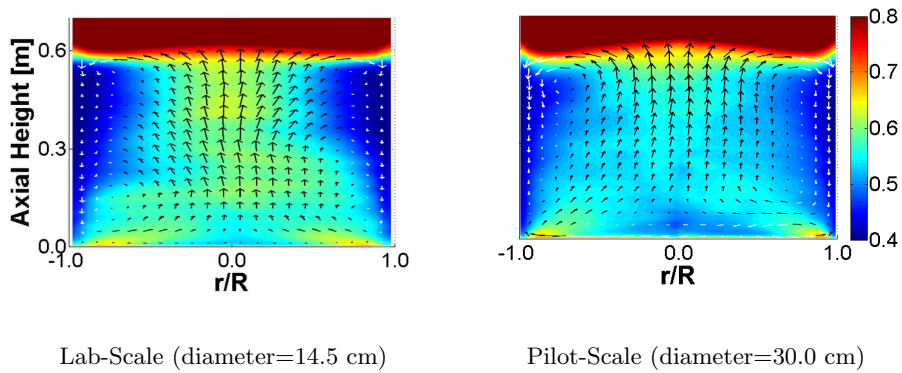
Figure 12: Comparison of the time and azimuthally averaged void fraction overlaid with solids velocity vectors (black - upwards, white - downwards) using ϕ=0.1 for U=18.86 cm/s (U/U$_{\mathrm{mf}}$=4.6) in the 14.5 cm lab and 30 cm pilot-scale beds. Velocity vectors are meant for illustration and vector-lengths may only be used as estimates for the magnitude
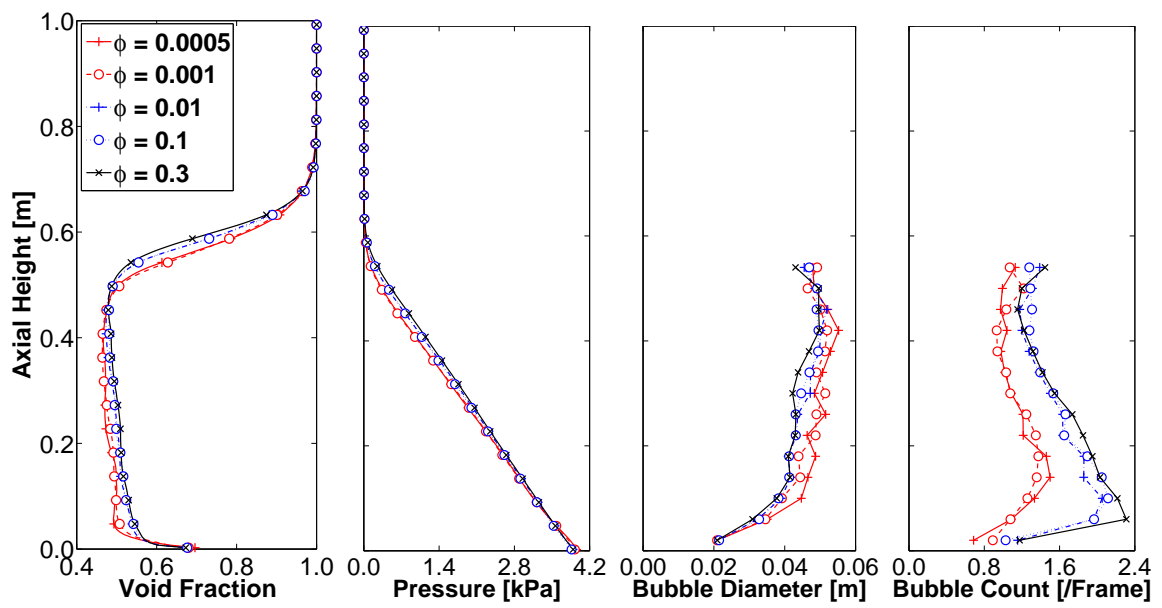
Figure 13: Time average gas-phase metrics using different values of ϕ
for U=18.86 cm/s in the 30 cm pilot-scale bed

33
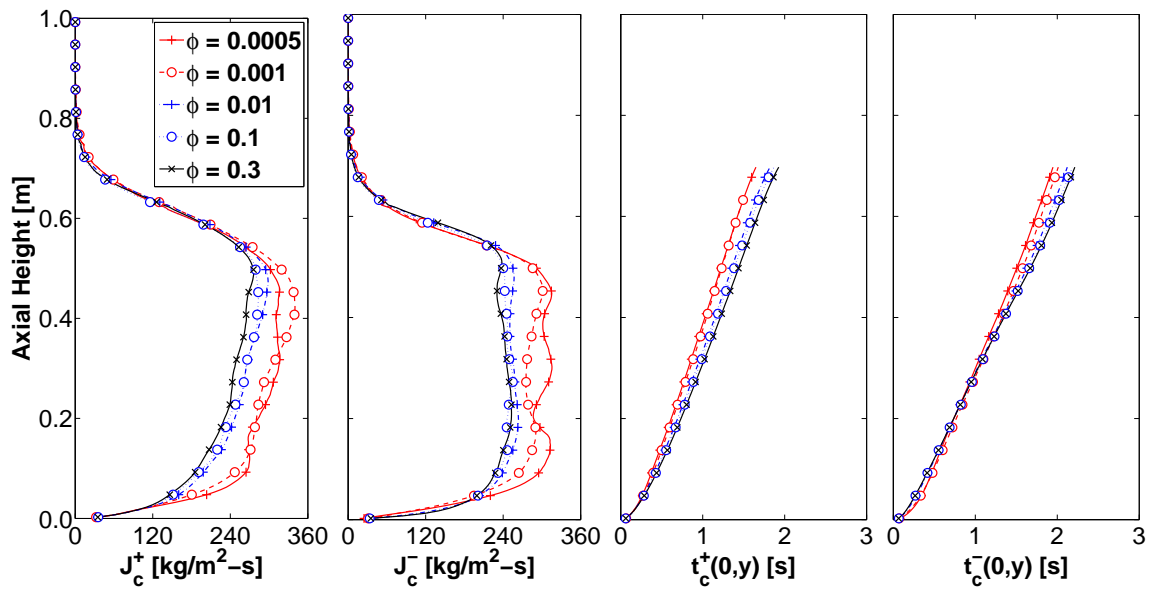
Figure 14: Time average solid-phase metrics using different values of ϕ
for U=18.86 cm/s in the 30 cm pilot-scale bed
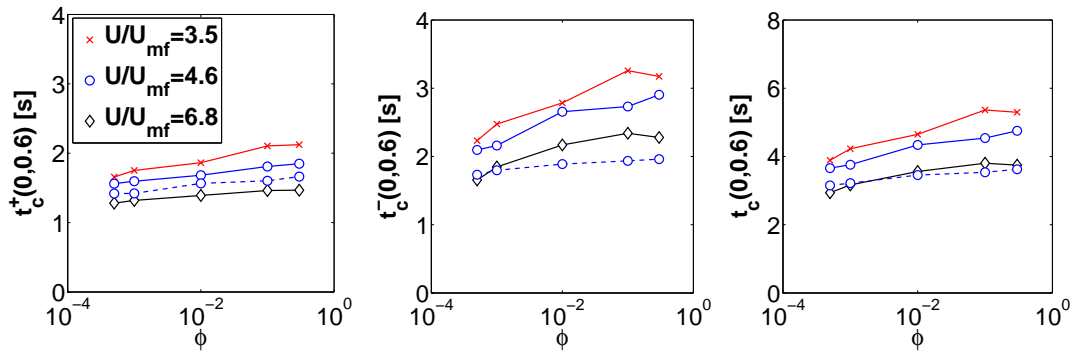
Figure 15: Variation of solids circulation times (t_c^+, t_c^- and t_c) with ϕ in the lab-scale bed (—) for U/U$_{\mathrm{mf}}$=3.5, 4.6 and 6.8 and comparison with the solids circulation time in the pilot-scale bed (−−) for U/U$_{\mathrm{mf}}$=4.6
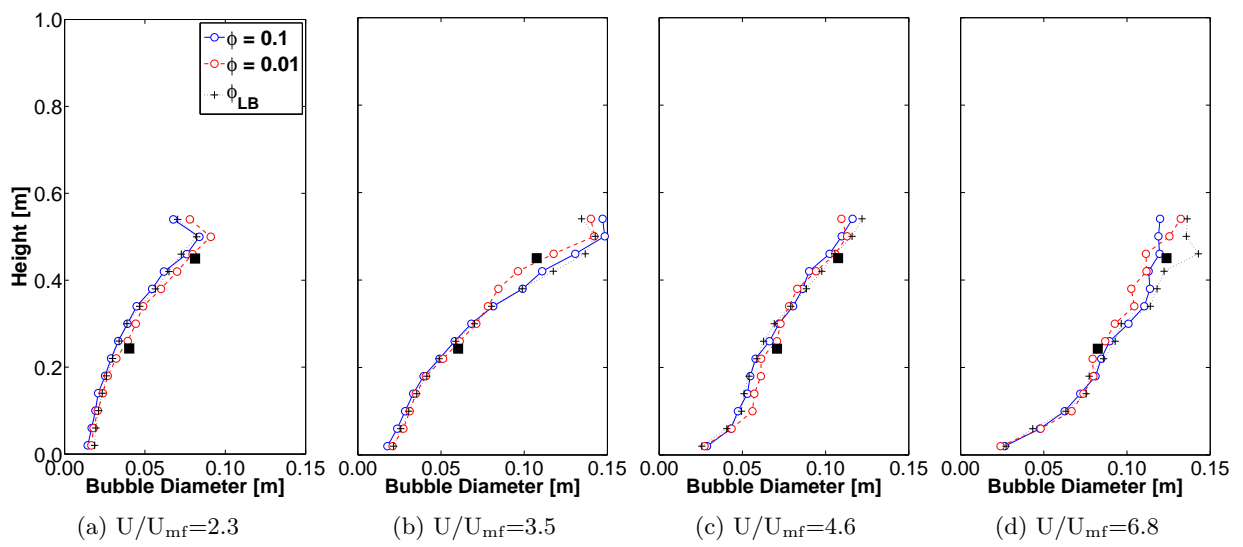
Figure 16: Comparison of average bubble diameters using ϕ predicted by Li and Benyahia (ϕ_{LB}) [1], ϕ=0.01 and ϕ=0.1 for U/U$_{\text{mf}}$=2.3, 3.5, 4.6 and 6.8 with experimental measurements (*filled squares*) by Rüdisüli et al [20] at two axial locations y=0.23 m and 0.45 m
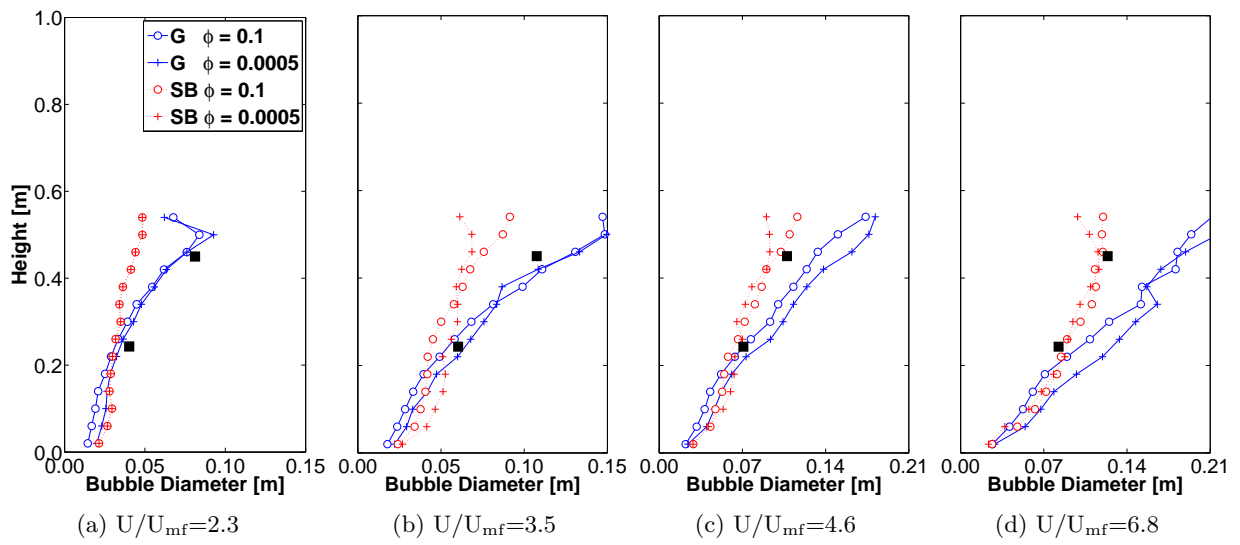
Figure 17: Comparison of average bubble diameters using Gidaspow (G) and Syamlal-O'Brien (SB) drag models for range of ϕ and U/U$_{mf}$=2.3, 3.5, 4.6 and 6.8 with experimental measurements (*filled squares*) by Rüdisüli et al [20] at two axial locations y=0.23 m and 0.45 m
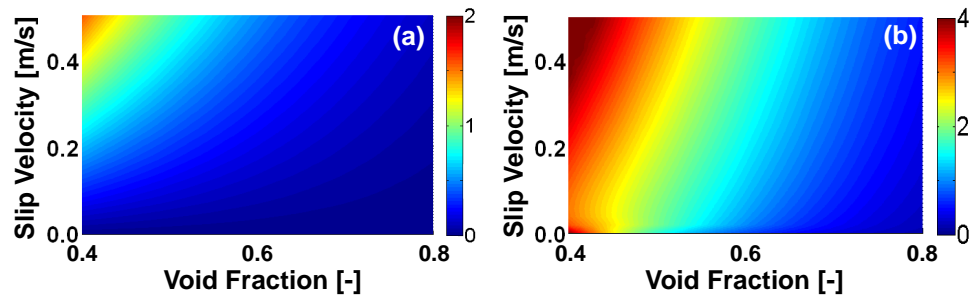
Figure 18: Comparison of computed drag forces (in 10^4 kg/m^2-s^2) using (a) Gidaspow model (Equations 6-9) and (b) Syamlal-O'Brien model (Equations 10-12) for Alumina particles (d$_p$=289 μm)
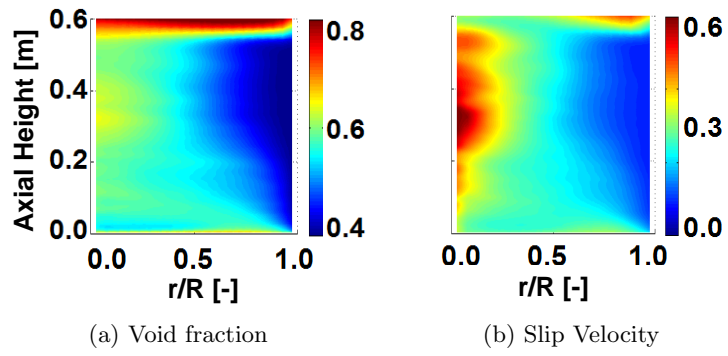
(a) Void fraction (b) Slip Velocity

Figure 19: Time and azimuthally averaged void fraction and solids-gas slip velocity in the bed for U/U$_{\mathrm{mf}}$=4.6 [20] using the Syamlal-O'Brien drag model and ϕ=0.01